



# A Subset of Oligodendrocyte Lineage Cells Interact With the Developing Dorsal Root Entry Zone During Its Genesis

Lauren A. Green<sup>1,2†</sup>, Robert M. Gallant<sup>1†</sup>, Jacob P. Brandt<sup>1</sup>, Ev L. Nichols<sup>1</sup> and Cody J. Smith<sup>1,2\*</sup>

<sup>1</sup> Department of Biological Sciences, University of Notre Dame, Notre Dame, IN, United States, <sup>2</sup> Center for Stem Cells and Regenerative Medicine, University of Notre Dame, Notre Dame, IN, United States

## OPEN ACCESS

### Edited by:

Wia Baron,  
University Medical Center Groningen,  
Netherlands

### Reviewed by:

Hirohide Takebayashi,  
Niigata University, Japan  
Fernando C. Ortiz,  
Autonomous University of Chile, Chile  
Lisbeth Schmidt Laursen,  
Aarhus University, Denmark

### \*Correspondence:

Cody J. Smith  
csmith67@nd.edu

† These authors have contributed  
equally to this work

### Specialty section:

This article was submitted to  
Non-Neuronal Cells,  
a section of the journal  
Frontiers in Cellular Neuroscience

Received: 10 March 2022

Accepted: 11 May 2022

Published: 06 June 2022

### Citation:

Green LA, Gallant RM, Brandt JP,  
Nichols EL and Smith CJ (2022) A  
Subset of Oligodendrocyte Lineage  
Cells Interact With the Developing  
Dorsal Root Entry Zone During Its  
Genesis.  
Front. Cell. Neurosci. 16:893629.  
doi: 10.3389/fncel.2022.893629

Oligodendrocytes are the myelinating cell of the CNS and are critical for the functionality of the nervous system. In the packed CNS, we know distinct profiles of oligodendrocytes are present. Here, we used intravital imaging in zebrafish to identify a distinct oligodendrocyte lineage cell (OLC) that resides on the dorsal root ganglia sensory neurons in the spinal cord. Our profiling of OLC cellular dynamics revealed a distinct cell cluster that interacts with peripheral sensory neurons at the dorsal root entry zone (DREZ). With pharmacological, physical and genetic manipulations, we show that the entry of dorsal root ganglia pioneer axons across the DREZ is important to produce sensory located oligodendrocyte lineage cells. These oligodendrocyte lineage cells on peripherally derived sensory neurons display distinct processes that are stable and do not express *mbpa*. Upon their removal, sensory behavior related to the DRG neurons is abolished. Together, these data support the hypothesis that peripheral neurons at the DREZ can also impact oligodendrocyte development.

**Keywords:** zebrafish, glia, oligodendrocyte, sensory neuron, development, DRG

## INTRODUCTION

Oligodendrocytes are the myelinating glial cell-type of the central nervous system. We know this myelination is essential for the classically described role of insulation that aids in saltatory conduction of neuronal information throughout the body (Nave and Werner, 2014; Allen and Lyons, 2018). Single-cell RNA sequencing approaches have now clearly demonstrated the heterogeneity among such oligodendrocytes (Marques et al., 2016). For example, scRNA sequencing of mature oligodendrocytes (OLs) in the mouse CNS defined 13 distinct populations of mature OLs (Marques et al., 2016). This data, and others, further identifies heterogeneity within subsets of mature OLs enriched in specific regions of the CNS (Marques et al., 2016; Spitzer et al., 2019; Marisca et al., 2020). In zebrafish, immature oligodendrocyte cells have also been described as heterogeneous in the spinal cord (Marisca et al., 2020). While it is now generally accepted that oligodendrocytes display some heterogeneity, the properties of such heterogeneous populations are less understood.

What we do know is that oligodendrocyte heterogeneity in the spinal cord and forebrain can be driven by distinct progenitors (Cai et al., 2005; Vallstedt et al., 2005; Kessarar et al., 2006; Richardson et al., 2006; Tripathi et al., 2011; Crawford et al., 2016; Naruse et al., 2016). In the spinal cord of mice most OPCs originate from common progenitors in the pMN but a subset of

OPCs also arise from *dbx*<sup>+</sup> cells that are positioned more dorsally in the spinal cord (Spassky et al., 1998; Cai et al., 2005; Fogarty et al., 2005; Vallstedt et al., 2005). The recent model of progenitor recruitment during oligodendrocyte specification, in zebrafish, may update the theory of dorsal versus ventral derived oligodendrocytes, indicating they both may migrate from the pMN domain but at temporally distinct times (Ravanelli and Appel, 2015). These studies may support origin and temporal derivation as drivers of heterogeneity. It is also clear that environmental events that OPCs experience while navigating to their mature location could impact heterogeneity. We know tiling, activity-dependent mechanisms and a plethora of signaling cascades impact oligodendrocyte differentiation, sheath production and survival (Kirby et al., 2006; Emery, 2010; Hughes et al., 2013; Nave and Werner, 2014; Hines et al., 2015; Mensch et al., 2015; Koudelka et al., 2016; Allen and Lyons, 2018). However, these developmental events have mostly been studied without the heterogeneity of oligodendrocytes as a focus.

Here, we utilize time-lapse imaging of zebrafish to characterize a distinct population of oligodendrocyte lineage cells (OLCs) that reside on sensory neurons in the spinal cord. Using this approach, we visualize a subpopulation of OPCs that migrate toward peripheral sensory neurons as their axons enter the spinal cord. These migrating OPCs contact the dorsal root entry zone (DREZ) and immediately migrate dorsally to associate specifically with CNS-located sensory nerves. These sensory-related OLCs exhibit and maintain unique molecular and process profiles and display a distinct response to OLCs tiling. In the absence of sensory-related OLCs, we observed an elimination of a behavioral response to a noxious stimulus. The identification of a population of sensory-associated OLCs with anatomical, developmental and functional heterogeneity from classically described oligodendrocytes adds insight to the heterogeneity of oligodendrocyte populations in the nervous system.

## RESULTS

### Profiling of *sox10*<sup>+</sup>-Spinal Cord Cell Dynamics Reveals a Sensory Associated OLC

To investigate OLC heterogeneity, we used time-lapse imaging of OLCs in the spinal cord of intact *Tg(sox10:mrfp)* zebrafish (Kirby et al., 2006). We considered that the migration of distinct OL progenitor cells could reveal heterogeneous OL populations. To explore this, we tracked individual oligodendrocyte progenitor cells (OPC) within 40  $\mu$ m spinal cord z-projections spanning 200  $\mu$ m in zebrafish from anterior/posterior as they migrated from their precursor domain to when they halted migration to produce oligodendrocyte sheaths. In this profiling, we measured the directional changes and total distance traveled of single oligodendrocytes (**Figure 1A**) ( $n = 6$  animals,  $n = 20$  OLCs). Even with just two parameters, *k*-means clustering analysis showed at least three clusters of distinct populations of OLCs, one of which includes cells that migrate less than 100  $\mu$ m with less than 2 directional changes, a second that includes cells migrating a

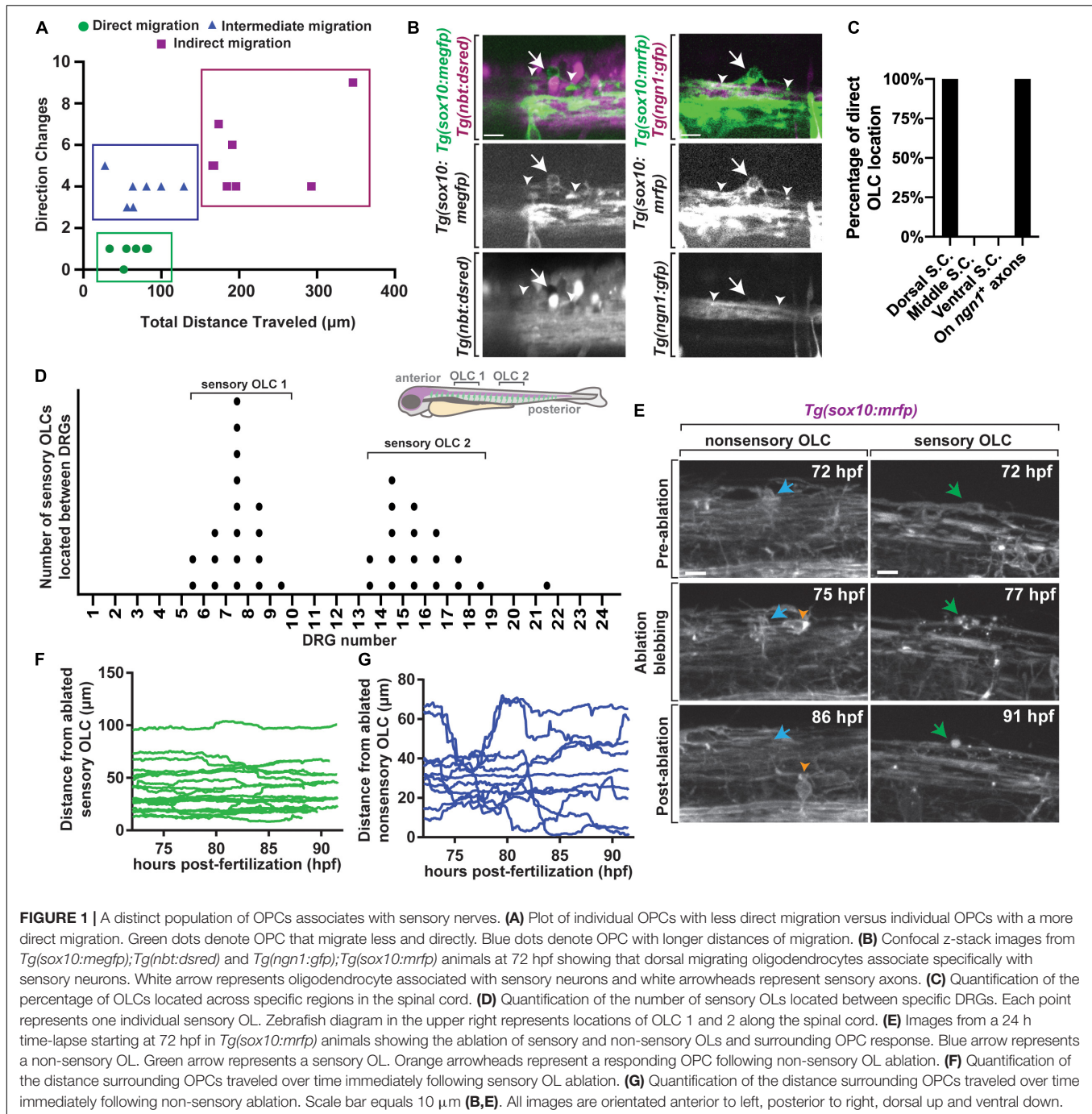
similar distance but with 3–5 directional changes and a third cluster that migrated with distances that varied from 165 to 350  $\mu$ m and greater than 3 directional changes (**Figure 1A**) ( $n = 6$  animals,  $n = 20$  OLCs).

To determine if these distinct migration patterns dictate potential heterogeneity of OLs we determined if such clusters corresponded with specific anatomically distinct populations. We noted that a cluster of migrating cells resided on the dorsal side of the spinal cord. To determine if they are associated with a specific neuronal population we marked subsets of neurons with specific transgenes. We first scored the location of the OLCs in *Tg(sox10:megfp); Tg(nbt:dsred)* animals which use regulatory sequences of *sox10* to mark oligodendrocytes and their progenitors and *nbt* to panneuronally label axons (**Figures 1B,C**) ( $n = 19$  animals total) (Peri and Nüsslein-Volhard, 2008; Smith et al., 2014). In this analysis, 100% of the direct-migration cluster resided on dorsally located *nbt*<sup>+</sup> tracts, indicating their association with neurons (**Figure 1C**) ( $n = 10$  animals with *nbt*). The location of these dorsal OLCs corresponded near the dorsal longitudinal fasciculus which contains Rohon Beard sensory neurons and DRG sensory neurons in zebrafish. To test if they resided on DRG sensory neurons we similarly scored their association in *Tg(ngn1:gfp); Tg(sox10:mrfp)* animals (Kirby et al., 2006; Prendergast et al., 2012), which mark DRG sensory neurons at 72 hpf as *ngn1*<sup>+</sup>; *sox10*<sup>+</sup>. Rohon Beard neurons, in contrast, do not express *sox10* (**Figures 1B,C**). 100% of the direct-migration cluster generated OLCs that reside on the DRG sensory neurons (**Figure 1C**) ( $n = 9$  animals with *ngn1*). Throughout the manuscript, we define sensory-related OLCs as *sox10*<sup>+</sup> cells that reside on the DRG sensory neurons and non-sensory-related OLCs as *sox10*<sup>+</sup> cells that are not located on the sensory neurons.

We further explored the anatomical positioning of sensory-related OLCs by scoring their location in the spinal cord. To do this, we created images that tiled the entirety of the right side of the spinal cord in *Tg(sox10:mrfp);Tg(ngn1:gfp)* animals, allowing us to identify the sensory neurons and the sensory associated OLCs. In this analysis, sensory associated OLCs were distinctly concentrated in two locations in the zebrafish spinal cord. These locations corresponded with DRGs 5–10 and 13–18, with each area having one sensory associated OLC per side of the spinal cord (**Figure 1D**) ( $n = 9$  animals). All our analysis below was completed at DRGs 6–10 to maximize our likelihood of visualizing these cells. Collectively, these data led us to further characterize at least one small subpopulation of anatomically distinct OLCs.

### Sensory-Related OLCs Are Not Replaced by Surrounding OPC Populations Following Ablation

It is well documented that OPCs intrinsically replenish damaged or apoptotic OLs to fill the newly vacant space following OL death (Kirby et al., 2006; Hughes et al., 2013). We therefore next asked if surrounding non-sensory-related OLC populations could replace an ablated sensory-related OLC. To test this, we ablated individual sensory-related OLCs in *Tg(sox10:mrfp)* animals and



imaged surrounding OL and OPC response from 72 to 96 hpf (**Figure 1E**) ( $n = 32$  animals) (Green et al., 2019). As a control for this, we also ablated individual non-sensory-related OLCs and imaged the surrounding OL response from 72 to 96 hpf. In cases of sensory-related OLC ablation, no surrounding *sox10*<sup>+</sup> cell responded to the site of ablation (**Figure 1F**) ( $n = 19$  animals). In cases of non-sensory OL ablation, surrounding *sox10*<sup>+</sup> cells immediately responded to the site of ablation as previously reported (**Figure 1G**) ( $n = 13$  animals). These data demonstrate a difference between the sensory subpopulation of

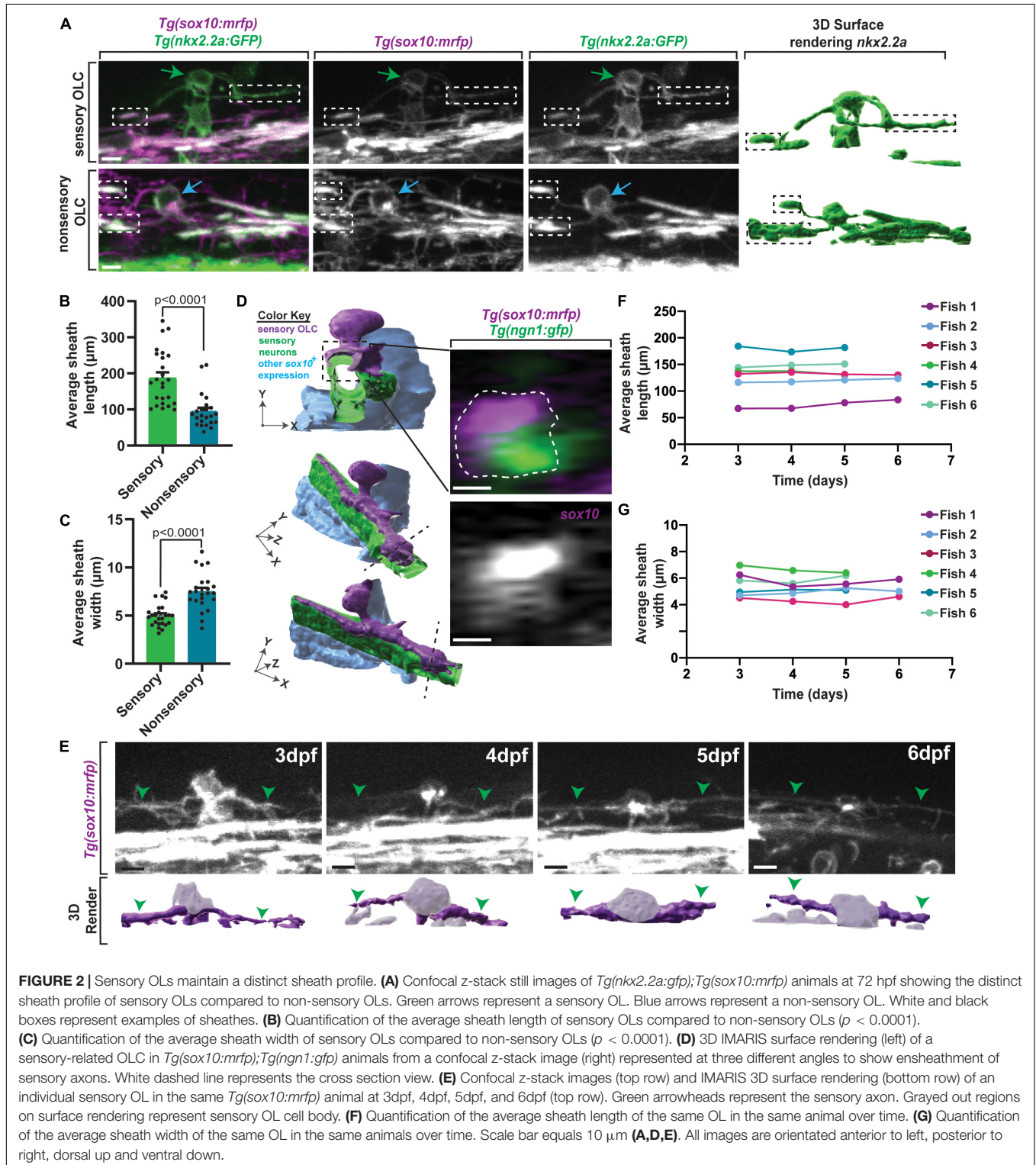
OLCs and non-sensory associated OLCs, as they are not replaced by surrounding OLCs.

## Sensory-Related OLCs Have Distinct Sheathes

We next tested if these sensory-related OLCs have other distinct structural properties by first measuring their cellular processes. We compared these processes to other classically described OLCs. To investigate this, we imaged sensory-related OLCs in

*Tg(nkx2.2a:gfp);Tg(sox10:mrfp)* animals at 72 hpf and measured the sheath width and sheath length of both sensory and classically described non-sensory-related OLCs (Figure 2A; Kirby et al., 2006). The average process length of sensory-related OLC was  $187.78 \pm 15.20 \mu\text{m}$  compared to an average of  $94.67 \pm 9.88 \mu\text{m}$

( $p < 0.0001$ ) for non-sensory OLCs, indicating sensory-related OLCs exhibit longer and thinner processes/sheathes than non-sensory OLCs (Figure 2B) ( $n = 12$  sensory-related OLC, 11 non-sensory-related OLC,  $p > 0.0001$ ). Additionally, the average width of sensory-related OLCs process was  $5.01 \pm 0.23 \mu\text{m}$



compared to an average of  $7.49 \pm 0.41 \mu\text{m}$  for non-sensory OLs, demonstrating that sensory-related OLCs have a distinct process profile compared to other non-sensory OLs (Figure 2C) ( $n = 12$  sensory-related OLC, 11 non-sensory-related OLC,  $p > 0.0001$ ).

Oligodendrocytes ensheath axonal domains whereas precursor and progenitor populations do not (Nave and Werner, 2014; Allen and Lyons, 2018). To determine if these unique processes ensheath, similar to other oligodendrocyte populations, we imaged *Tg(ngn1:gfp); Tg(sox10:mrfp)* animals at 3 dpf. These animals label sensory neurons in GFP and mRFP and sensory-related OLC in mRFP. We then reconstructed the surfaces of the cells and digitally rotated the images. In these images, mRFP cell membrane can be visualized outside and ensheathed around GFP; mRFP axons, likely indicating ensheathment of the axon. These data indicate the sensory-related OLC at 3 dpf have at least initiated ensheathment of axons, likely designating them as oligodendrocytes, albeit by current definitions (Figure 2D). Furthermore, time-lapse imaging with *Tg(sox10:mrfp)* animals revealed that oligodendrocyte lineage cells located on sensory axons do not divide, at least during our 24 h imaging windows, potentially arguing again against them representing an immature progenitor or precursor cell.

It is possible that the difference in processes was an indication of immaturity, where sensory-associated OLC represent less mature cells. In zebrafish, classically described oligodendrocytes do not change the number of myelin sheathes after the first 3 h of ensheathment (Watkins et al., 2008; Czopka et al., 2013). We therefore asked if this distinct cellular process profile in sensory-associated OLCs is maintained over time. To test this, we located one sensory-related OLC in individual *Tg(nkx2.2a:gfp); Tg(sox10:mrfp)* animals at 3 dpf. We then imaged that same sensory-related OLC per animal at 4 dpf, 5 dpf, and 6 dpf, far exceeding the published 3-h window of sheath dynamics (Figure 2E) ( $n = 6$  animals) (Watkins et al., 2008; Czopka et al., 2013). To ask if individual cellular processes themselves were stable, we measured the length and width of the individual processes. These measurements showed the average process length per sensory-related OLC per animal was maintained from 3 to 6 dpf (Figure 2F) (fish 1  $p = 0.8621$ , fish 2  $p = 0.9969$ , fish 3  $p = 0.9988$ , fish 4  $p = 0.9217$ , fish 5  $p = 0.9604$ , fish 6  $p = 0.9562$ ). Similarly, these measurements also showed the average process width per sensory-related OLC per animal was maintained from 3 to 6 dpf (Figure 2G) (fish 1  $p = 0.7275$ , fish 2  $p = 0.9834$ , fish 3  $p = 0.9207$ , fish 4  $p = 0.9375$ , fish 5  $p = 0.9890$ , fish 6  $p = 0.9574$ ). While the length and width of the sheathes did not change overtime, a flattening of the cell body could be visualized (Figure 2E). Overall, this data shows that sensory-related OLCs have a cell-process profile that is maintained over time.

## Sensory Associated OLCs Are Produced From the Same Spinal Domain as Other OLCs

To uncover potential events that impact sensory-related OLCs production we first considered the possibility that sensory-related OLCs were produced from different oligodendrocyte precursors or progenitors that precedes their arrival to the

sensory neurons. In the spinal cord, current literature states that the majority of oligodendrocytes are produced from the *olig2*<sup>+</sup> pMN with a subset potentially produced from a more dorsal *dbx*<sup>+</sup> pMN domain (Richardson et al., 2006). To determine if these cells are derived from progenitors from different domains we used transgenic markers consistent with different regions of the spinal cord (Supplementary Figure 1A). In this analysis, 100% of the sensory associated OLCs expressed *Tg(sox10:mrfp)* and *Tg(sox10:megfp)* that label OPCs and oligodendrocyte (Supplementary Figure 1B) ( $n = 25$  animals total). *Tg(dbx:gfp)* labeled 0% of sensory-associated OLCs, indicating that these sensory oligodendrocytes unlikely directly originated from the *dbx*<sup>+</sup> region of the spinal cord ( $n = 7$  animals) (Briona and Dorsky, 2014). *Tg(nkx2.2a:gfp)* labeled 50% of the sensory-associated OLC indicating a subset originated from the area around the floor plate region of the spinal cord ( $n = 8$  animals). All the sensory-associated OLCs were labeled with *Tg(olig2:dsred)* specifying they originated from the pMN domain of the spinal cord like other oligodendrocyte populations ( $n = 7$  animals) (Park et al., 2002). These data, in conjunction with previous literature, support the conclusion that both sensory and non-sensory-related OLC are derived from the same spinal domain.

If these sensory-related OLCs are derived from the pMN domain like other oligodendrocytes, then their migration should originate from those ventral spinal domains. We tested this possibility with a second complementary assay by photoconverting OPCs in the ventral spinal region. To trace the direct migration of a single cell to the sensory axon from the ventral spinal cord region, we used *Tg(sox10:eos)* to photoconvert all ventral OPCs and imaged migration from 48 to 72 hpf (Supplementary Figure 1C) ( $n = 3$  animals) (McGraw et al., 2012; Green and Smith, 2018). We observed photoconverted (red) cells migrate dorsally from the ventral spinal cord directly to the sensory axon (Supplementary Figure 1D). These data are inconsistent with the conclusion that the sensory-related OLCs are a result of production from different spinal cord precursor/progenitor domains, at least defined by current spinal domain literature.

## Sensory-Related OLCs Interact With the Dorsal Root Entry Zone

We next considered the hypothesis that their migration exposed them to unique spatiotemporal experience. We noted in timelapse movies that these directed OPCs migrated dorsally and halted their migration in the dorsal spinal cord, close to the dorsal root entry zone (DREZ) (Smith et al., 2017). We therefore asked if this cluster of OPCs contact the DREZ during migration. To test this, we imaged *Tg(sox10:gal4;uas:lifect-gfp)* zebrafish which allow us to visualize thin projections from the OPCs and sensory neurons during pioneer axon entry (Hines et al., 2015; Nichols and Smith, 2019a,b; Zhang et al., 2019). Since axon entry occurs between 48 and 72 hpf we also quantified the number of OPCs located on sensory nerves from 36 to 96 hpf (Figures 3A,B) ( $n = 20$  animals). No OPCs were present on sensory axons from 36 to 48 hpf, however, an average of  $0.57 \pm 0.291$  OPCs were present on sensory axons from 48 to 72 hpf and an average of

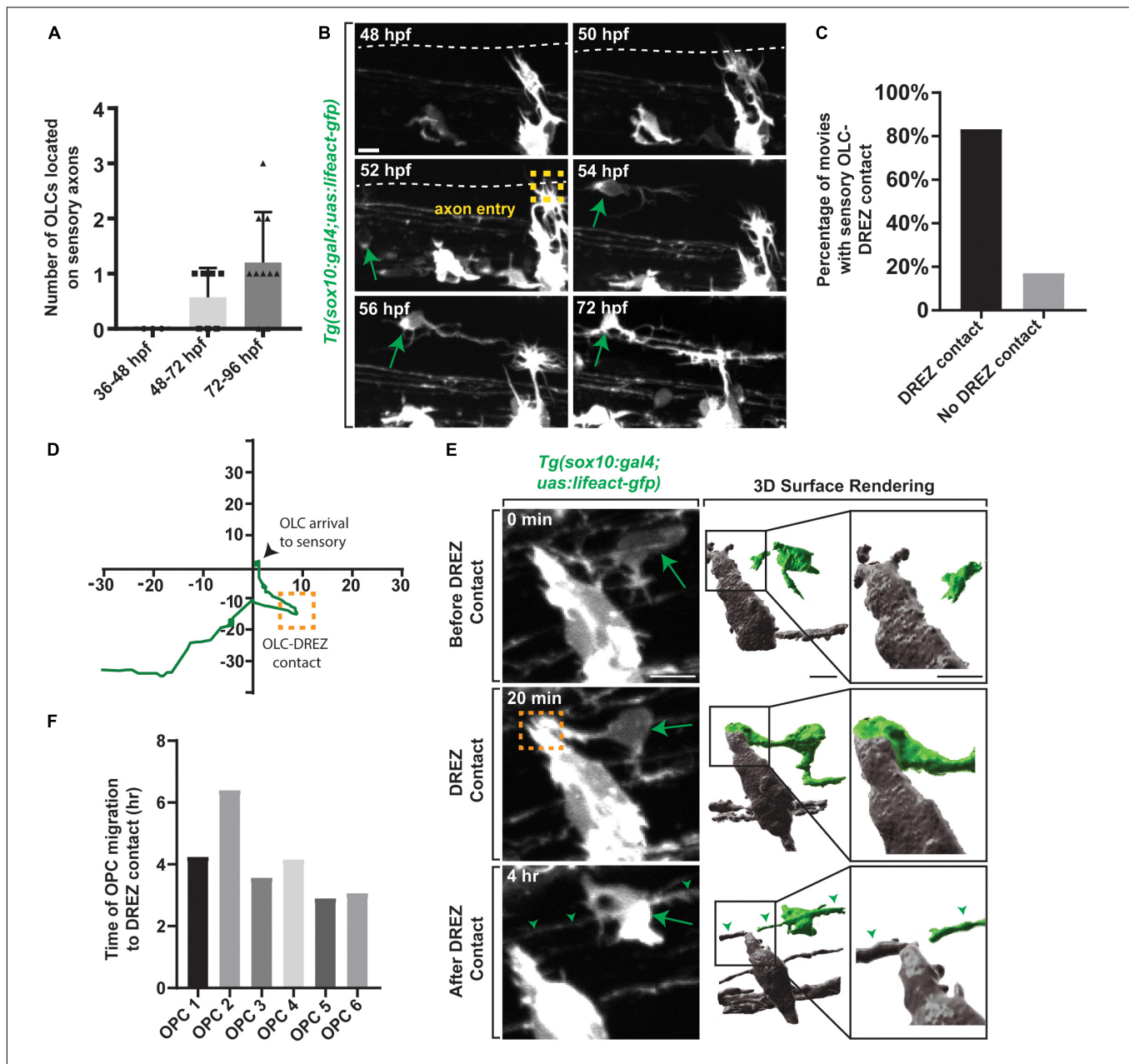


**FIGURE 3** | Oligodendrocyte progenitor cells contact the DREZ immediately following axon entry. **(A)** Quantification of the number of OPCs located with DRG sensory nerves from 36 to 96 hpf. **(B)** Images from a 24 h time-lapse movie starting at 48 hpf in *Tg(sox10:gal4; uas:lifect-gfp)* zebrafish showing OPC migration initiation following axon entry. Green arrow represents migrating OPC. Yellow box represents axon entry. **(C)** Quantification of the percentage of movies where oligodendrocytes arrived to the sensory with or without DREZ contact. **(D)** Migration plot of the path an oligodendrocyte traveled from the ventral spinal cord region to sensory axons. Orange box represents DREZ contact. **(E)** Images from a 24 h time-lapse movie starting at 48 hpf in *Tg(sox10:gal4; uas:lifect-gfp)* zebrafish showing an oligodendrocyte extending a cellular process that contacts the DREZ. Green arrow represents OPC projection that contacts the DREZ. Orange box indicates OPC-DREZ contact. Green arrowheads represent the sensory axon. IMARIS 3D surface rendering of the 20 min confocal image in showing an OLC cellular process contacting the DREZ. Gray cells are DRG and peripherally located. Green cell is the sensory OL. **(F)** Quantification of the time it takes for an individual OPC to initiate migration post-axon entry and contact the DREZ. Scale bar equals 10  $\mu\text{m}$  (**B,E**). All images are orientated anterior to left, posterior to right, dorsal up and ventral down.

$1.2 \pm 0.202$  OPCs were present from 72 to 96 hpf (**Figures 3A,B**) ( $n = 20$  animals). Our data further indicate that 80% of OPCs in the directed cluster contacted the DREZ before they halted their migration and produced sheathes on sensory axons (**Figure 3C**) ( $n = 6$  animals). After DREZ contact, these OPCs migrated an

average of  $17.10 \mu\text{m}$  dorsally until they halted further migration (**Figure 3D**) ( $n = 6$  animals).

Unlike other events that have been identified to promote oligodendrocyte development, the DREZ is composed of peripheral nervous system components (Golding et al., 1997;

Smith et al., 2017), making it somewhat surprising that it could influence CNS development. To begin to address the role of the DREZ in sensory-related OLCs we assessed when the DREZ-directed OPCs contact the DREZ. For this study, we define the genesis of the DREZ as the time in development when the peripheral nervous system derived pioneer DRG axons enter the spinal cord from their peripheral location (Nichols and Smith, 2019a). In zebrafish, this occurs between 48 and 72 hpf. The precise spatiotemporal location of pioneer axon entry and DREZ genesis can be identified by the formation of actin-based invasive structures in pioneer axons (Nichols and Smith, 2019a,b; Zhang et al., 2019; Kikel-Coury et al., 2021). To ask if DREZ-directed OPCs contact the DREZ during this process we collected z-stacks every 5 min from 48 to 72 hpf in *Tg(sox10:gal4; uas:lifect-GFP)* animals (Figures 3E,F) ( $n = 6$  animals). In these animals, both oligodendrocytes and sensory neurons are labeled with Lifect-GFP but separated spatially, with OLCs in the spinal cord and sensory neurons in the periphery. We imaged the spinal section where one sensory-related OLC is present per animal. In these movies, 100% of the DREZ-directed OPCs contacted the DREZ after the axons had entered the spinal cord, contacting the peripheral portion of the cells at the DREZ (Figure 3E and Supplementary Figure 2A) ( $n = 6$  animals). Collectively in the movies, OPC DREZ-contact occurred 4.06 h after pioneer axon entry at the DREZ (Figure 3F) (Average time of OPC migration to DREZ per OPC: OPC 1 = 4.25, OPC 2 = 6.40, OPC 3 = 3.58, OPC 4 = 4.16, OPC 5 = 2.91, OPC 6 = 3.08). These results led us to the hypothesis that formation of the DREZ could impact the migration of OPCs from their ventral progenitor.

## Formation of the DREZ Is Required to Produce Sensory-Related OLCs

If the genesis of the DREZ directs sensory-related OLCs, then perturbing DREZ formation should alter the production of these sensory-related OLCs. To test this, we altered DREZ formation by disrupting DRG pioneer axons from entering the spinal cord as previously reported (Nichols and Smith, 2019a,b; Zhang et al., 2019). We first did this by blocking DRG pioneer axon entry components using SU6656, an inhibitor of Src that is required for pioneer axons to enter the spinal cord (Nichols and Smith, 2019a). In this experiment *Tg(sox10:mrfp); Tg(ngn1:gfp)* animals were treated with SU6656 or DMSO from 36 to 72 hpf to block axon entry (Figures 4A,B) ( $n = 27$  animals total) (Nichols and Smith, 2019a). We imaged a spinal region in these animals that spanned DRGs at somites 6–10 in which we know sensory-related OLCs are located and scored the number of sensory-related OLCs present (Figure 4C) ( $n = 8$  animals). In DMSO-treated spinal segments, an average of  $0.875 \pm 0.085$  sensory-related OLCs were present by 72 hpf ( $n = 16$  animals). This was in contrast to an average of  $0.091 \pm 0.090$  sensory OLCs that were present in SU6656-treated spinal segments where DREZ formation was perturbed ( $n = 11$  animals) (Figure 4C,  $p < 0.0001$ ). These results support the conclusion that failure to form the DREZ could result in reduced migration of OPCs to the sensory axons.

Since this pharmacological treatment is not cell-specific and therefore could impact OPC migration, we also used

complementary physical manipulations to test the requirement of DREZ formation to drive sensory-related OLCs. In this paradigm, pioneer axon entry was prevented by ablating the DRG neurons before they produce their pioneer axons and imaged as in our pharmacological experiments (Figures 4D,E) ( $n = 19$  animals total). In control spinal segments where the DRG pioneer neuron was not ablated, an average of  $0.93 \pm 0.077$  sensory-related OLCs were present at intact spinal segments ( $n = 13$  animals). This was a stark contrast to spinal segments where the pioneer neurons were ablated, in which we could not detect any sensory-related OLCs ( $n = 6$  animals) (Figure 4F,  $p < 0.0001$ ). We could identify the centrally-located DRG axon in DRG ablated animals because adjacent regions to the four-ablated nerves still entered and produced spinal projections.

We extended this analysis by altering the DREZ formation with a third complementary approach. Rac1 activation drives the disassembly of invasive structures and thus by mosaically expressing photoactivatable Rac1 in pioneer neurons and photo activating them during DREZ formation, we can block entry of pioneer axons into the spinal cord (Nichols and Smith, 2019a; Zhang et al., 2019). We injected animals with photoactivatable Rac1 protein at the single-cell stage and imaged *Tg(uas:lifect-gfp); Tg(sox10:gal4) uas:PA-Rac-mcherry* animals from 48 to 72 hpf (Figures 4G,H) ( $n = 18$  animals total) (Nichols and Smith, 2019a; Zhang et al., 2019; Kikel-Coury et al., 2021). Mosaic animals that were selected for this experiment contained PA-Rac-mcherry in the DRG neurons but not sensory-related OLCs, allowing us to manipulate the sensory ingrowth without impacting OLCs directly with Rac1 (Figure 4I). In control animals where the PA-Rac protein was injected, but not photoactivated with 445 nm, an average of  $1.0 \pm 0.111$  sensory-related OLCs could be detected in spinal segments ( $n = 9$  animals). In contrast, sensory-related OLCs could not be identified in spinal segments with photoactivated Rac1 ( $n = 9$  animals) (Figure 4I,  $p < 0.0001$ ). The simplest explanation for the data from these three manipulations of DREZ formation is consistent with the possibility that DREZ formation is important to produce sensory associated OLCs.

If the formation of the DREZ drives production of distinct OLCs, then altering the timing of DREZ formation should also change the timing of DREZ-directed OPCs and formation of sensory-related OLCs. To address this possibility, we induced early entry of pioneer axons by forcing the formation of invasive structures in pioneer DRG axons as previously noted (Figure 5A) ( $n = 8$  animals). To do this, we treated *Tg(sox10:gal4; uas:lifect-gfp)* animals with paclitaxel, a potent activator of invasive structures, from 36 to 72 hpf, then imaged them from 48 to 72 hpf (Figures 5A,C,D) ( $n = 8$  animals) (Nichols and Smith, 2019a,b; Kikel-Coury et al., 2021). To first confirm that pioneer axons entered the spinal cord early we scored the timing of pioneer axon entry. We normalized these time points in DMSO and Paclitaxel treated animals by scoring the time of entry compared to the initiation of the pioneer axon. Consistent with previous reports (Nichols and Smith, 2019a,b; Kikel-Coury et al., 2021), paclitaxel-treated animals had early genesis of the DREZ of  $2.33 \pm 0.439$  h on average compared to DMSO-treated animals where DREZ genesis occurred at

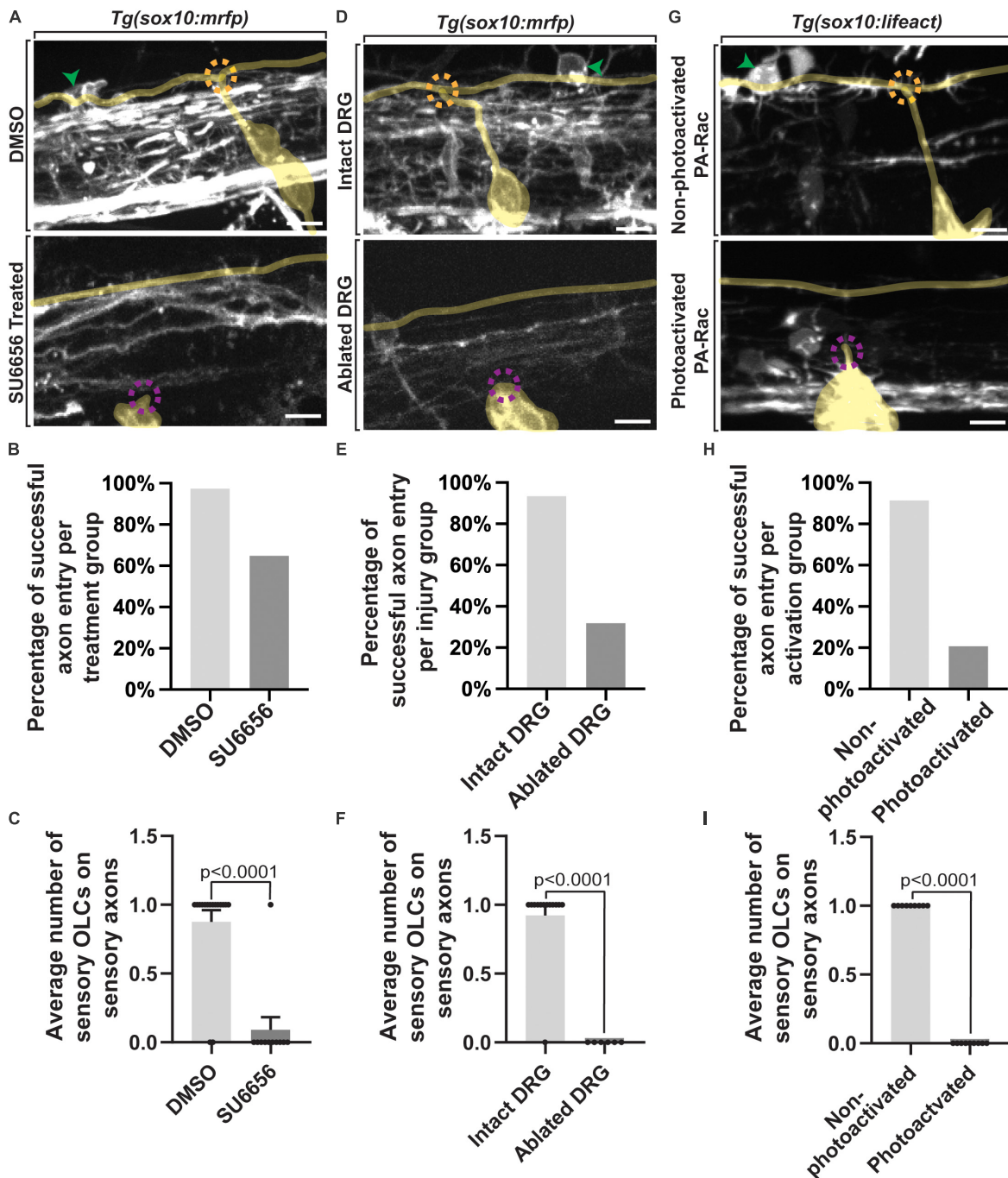


**FIGURE 4 |** Failed axon entry does not result in sensory-related OLCs. **(A)** Confocal z-stack images of *Tg(sox10:mrfp); Tg(ngn1:gfp)* zebrafish at 3 dpf showing axon entry and the presence or absence of a sensory-related OLC in DMSO control animals compared to SU6656 treated animals. **(B)** Quantification representing the percentage of successful axon entry events per DMSO group versus SU6656 treatments. **(C)** Quantification of the average number of sensory-related OLCs on sensory axons in DMSO versus SU6656 treated animals ( $p < 0.0001$ ). **(D)** Confocal z-stack images of *Tg(sox10:mrfp); Tg(ngn1:gfp)* zebrafish at 3 dpf showing axon entry and the presence or absence of a sensory OL in intact animals compared to animals with ablated DRGs. **(E)** Quantification representing the percentage of successful axon entry events per intact group versus ablated DRGs. **(F)** Quantification of the average number of sensory OLCs on sensory axons in intact DRGs versus ablated DRGs ( $p < 0.0001$ ). **(G)** Confocal z-stack images of *Tg(sox10:gal4; uas:lifect-gfp)* animals injected with PA-Rac1 at 3 dpf showing axon entry and the presence or absence of a sensory-related OLC in non-photoactivated animals compared to photoactivated animals. **(H)** Quantification representing the percentage of successful axon entry events per non-photoactivated group versus the photoactivated group. **(I)** Quantification of the average number of sensory-related OLCs on sensory axons in non-photoactivated versus photoactivated animals ( $p < 0.0001$ ). All green arrowheads represent sensory-related OLCs. All dashed orange circles represent successful axon entry. All dashed magenta circles represent failed axon entry. Yellow tracing overlays highlight the DRG and sensory axons **(A,D,G)**. Scale bar equals 10  $\mu\text{m}$  **(A,D,G)**. All images are orientated anterior to left, posterior to right, dorsal up and ventral down.

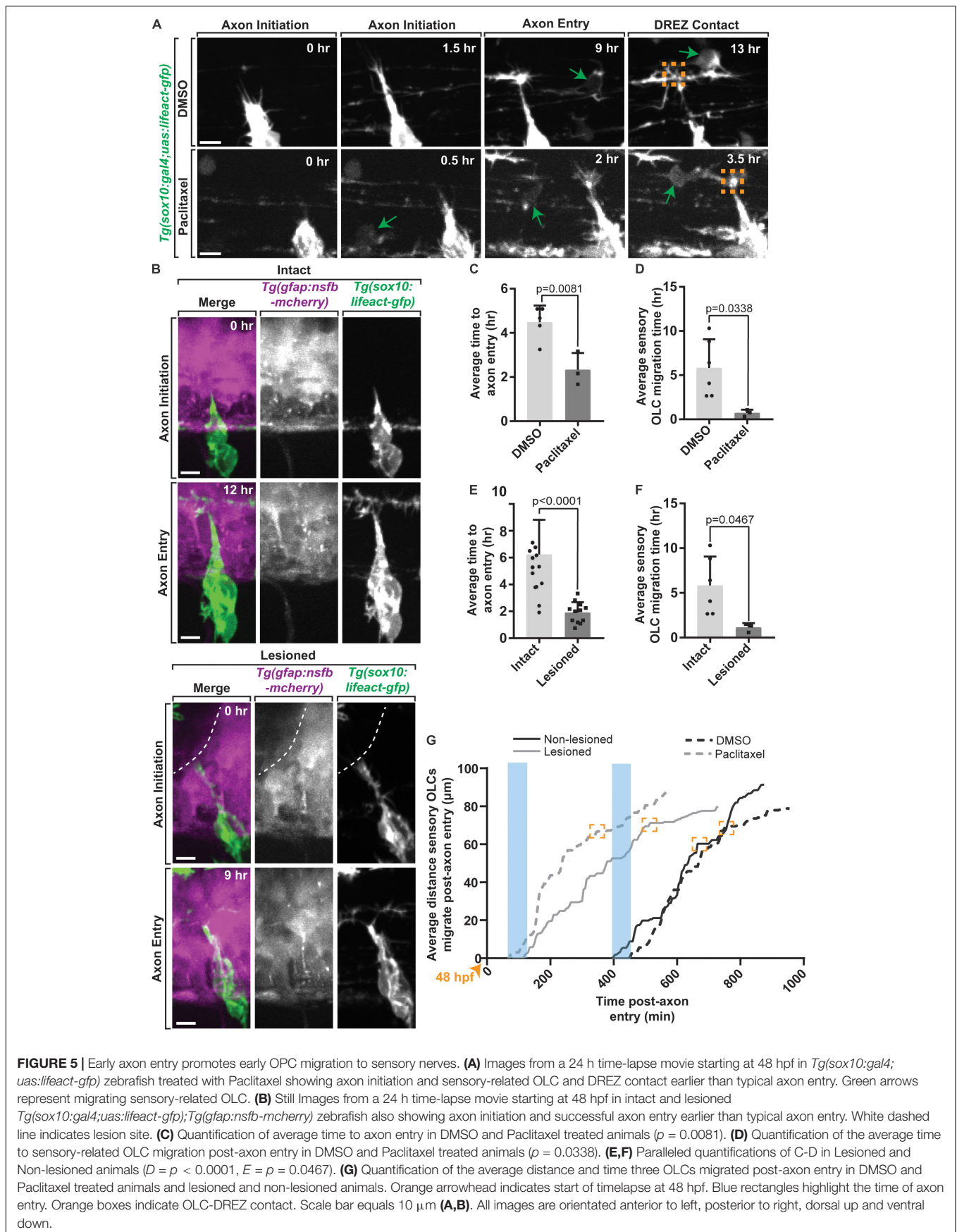


**FIGURE 5 |** Early axon entry promotes early OPC migration to sensory nerves. **(A)** Images from a 24 h time-lapse movie starting at 48 hpf in *Tg(sox10:gal4; uas:lifact-gfp)* zebrafish treated with Paclitaxel showing axon initiation and sensory-related OLC and DREZ contact earlier than typical axon entry. Green arrows represent migrating sensory-related OLC. **(B)** Still Images from a 24 h time-lapse movie starting at 48 hpf in intact and lesioned *Tg(sox10:gal4; uas:lifact-gfp); Tg(gfap:nsfb-mcherry)* zebrafish also showing axon initiation and successful axon entry earlier than typical axon entry. White dashed line indicates lesion site. **(C)** Quantification of average time to axon entry in DMSO and Paclitaxel treated animals ( $p = 0.0081$ ). **(D)** Quantification of the average time to sensory-related OLC migration post-axon entry in DMSO and Paclitaxel treated animals ( $p = 0.0338$ ). **(E, F)** Paralleled quantifications of C-D in Lesioned and Non-lesioned animals ( $D = p < 0.0001$ ,  $E = p = 0.0467$ ). **(G)** Quantification of the average distance and time three OLCs migrated post-axon entry in DMSO and Paclitaxel treated animals and lesioned and non-lesioned animals. Orange arrowhead indicates start of timelapse at 48 hpf. Blue rectangles highlight the time of axon entry. Orange boxes indicate OLC-DREZ contact. Scale bar equals  $10 \mu\text{m}$  **(A, B)**. All images are orientated anterior to left, posterior to right, dorsal up and ventral down.

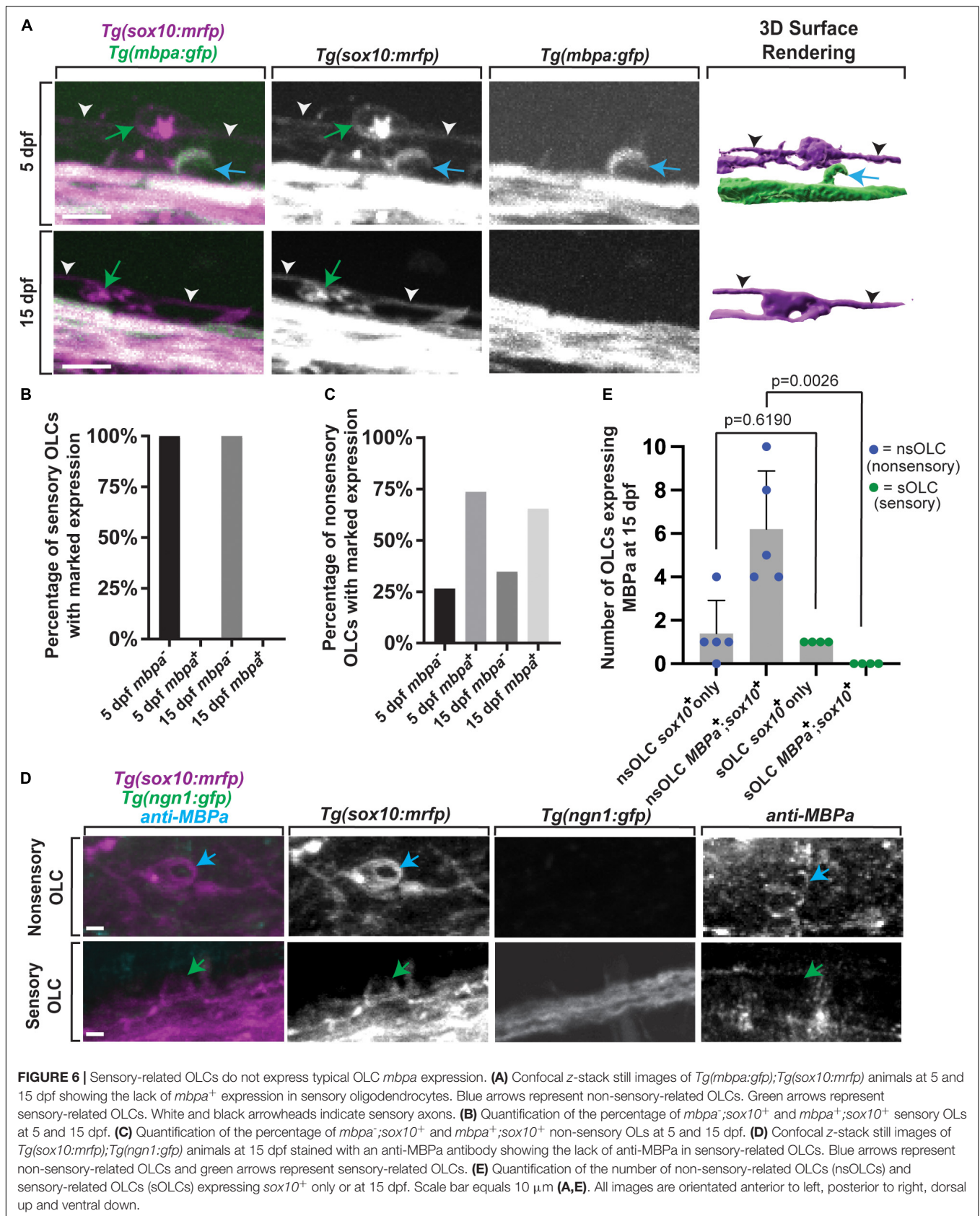
4.48 ± 0.338 h on average (**Figure 5C**,  $p = 0.0081$ ) ( $n = 8$  animals). In support of the hypothesis that DREZ formation drives the production of sensory-related OLCs, paclitaxel-treated animals formed DREZ-directed OPCs at 0.71 ± 0.217 h compared to DMSO that formed at 5.71 ± 1.322 h on average (**Figures 5D,G**) ( $p = 0.0338$ ,  $n = 8$  animals). As an argument against the possibility that this accelerated OPC migration was a result of increased velocity of OPCs, we tracked individual DREZ-directed OPCs as they migrated. The velocity of OPC migration in DMSO treated animals was 0.15 ± 0.037 on average compared to 0.08 ± 0.030 in paclitaxel-treated animals (**Supplementary Figure 2B**,  $p = 0.3001$ ,  $n = 8$  animals). The duration of time between initiation of OPC migration and arrival to the DREZ in DMSO-treated animals was 4.50 ± 0.936 h on average compared to 1.58 ± 0.096 h in paclitaxel-treated animals (**Supplementary Figure 2C**,  $p = 0.0710$ ,  $n = 8$  animals). Both the velocity and time of OPC migration were statistically indistinguishable. Together, these data support the possibility that OPCs migrate earlier when the DRG pioneer axons enter the DREZ early.

We next considered the possibility that the peripherally derived sensory pioneer axon itself could provide a cue to drive sensory-related OLCs. Alternatively, the actual act of the sensory axon breaching the radial glial limitans to cross into the spinal cord could drive the formation of these sensory-related OLCs. To provide insight into these two possibilities, we sought to mimic this potential breach by creating a break in the radial glial limitans with a physical manipulation (Nichols and Smith, 2019a). In this paradigm, we created a lesion of the radial glial limitans in a 10–12 μm region of the spinal cord directly dorsal to the motor exit point where the DREZ consistently forms, prior to pioneer axon initiation in *Tg(sox10:megfp)*; *Tg(gfap:mcherry)* animals at 48 hpf (Nichols and Smith, 2019a). After ablation, we imaged the radial glia lesion site from 48 to 72 hpf and quantified the time of axon initiation to axon entry, or DREZ formation in lesioned and non-lesioned animals (**Figures 5B,E–G**) ( $n = 9$  animals total). On average, axons enter in non-lesioned animals at 6.24 ± 0.712 h compared to 1.90 ± 0.225 h in lesioned animals (**Figure 5E**,  $p < 0.0001$ ). We then compared the timing of sensory-related OLC formation and DREZ contact of the OPC. Tracing DREZ directed OPC-cells in these movies revealed that creating an artificial breach of the spinal cord induced OPC-directed migration at an average of 2.0 ± 0.282 h compared to non-lesioned regions that migrated at an average of 6.0 ± 1.322 h (**Figure 5F**,  $p = 0.0467$ ). Arguing against the possibility that this expedited OPC migration was from increased velocity of the OPCs in the control versus experimental paradigm, the time for OPC migration from its initiation to the DREZ or velocity during that time was not significantly different (**Supplementary Figures 2D,E**,  $p = 0.5592$  and  $p = 0.5445$ ). Collectively, we observed accelerated OPC initiation of migration was in both Paclitaxel-treated and physically breached animals compared to DMSO-treated and non-breached animals (**Figure 5G**). Although we cannot distinguish between the possibility that sensory OPCs are instructed by sensory neurons versus triggered by the disruption of the glial limitans, we did quantify additional behaviors of sensory and non-sensory OPCs in taxol treated and physically breached animals. In lesioned animals, an average of

2.25 ± 2.0 non-sensory OPCs migrated within 50 μm of the DREZ compared to intact, DMSO treated, and Paclitaxel treated animals (**Supplementary Figures 2F,G**,  $p = 0.0203$ ,  $p > 0.9999$ ). This data suggests the physical breach of the DREZ does elicit an increase in non-sensory OLC migration, however, we did not observe any differences in the number of sensory OLCs. To test whether the physical breaching of the glial limitans may influence the behavior of migrating OPCs, we also quantified the maximum number of dynamic projections created by individual sensory and non-sensory OPCs during their migration to the DREZ in both lesioned animals and Paclitaxel treated animals. We did not detect any changes when compared to their respective intact or DMSO treated controls (**Supplementary Figures 2H–J**,  $p = 0.5370$ ,  $p = 0.6433$ ,  $p = 0.2134$ ,  $p = 0.5801$ ). The simplest explanation for this data is that the act of pioneer axon entry impacts DREZ-directed OPCs.

### Sensory-Related OLCs Have Distinct Molecular Properties to Non-sensory-related OLCs

Given the distinct sheath profile and development of sensory-related OLCs, we next asked whether these cells express myelin-associated factors distinct of other mature myelinating oligodendrocyte (Nave and Werner, 2014). To test this, we imaged *Tg(mbpa:gfp)*; *Tg(sox10:mrfp)* animals at 5 dpf and 15 dpf and scored the number of sensory-associated OLCs that were *mbpa*<sup>+</sup> (**Figure 6A**) ( $n = 55$  animals total) (Koudelka et al., 2016). We observed 100% of sensory-related OLCs at 5 dpf animals were *sox10*<sup>+</sup>, but 0% were *mbpa*<sup>+</sup> at 5 dpf (**Figure 6B**,  $n = 9$ , 5 dpf animals). To argue against the possibility that these cells presented immature *mbpa*<sup>+</sup> cells, we also imaged the same *Tg(mbpa:gfp)*; *Tg(sox10:mrfp)* animal at 5 dpf and 15 dpf, which again extends past the typical differentiation period of an oligodendrocyte in zebrafish (Czopka et al., 2013). At 15 dpf, we observed 100% sensory-related OLCs that were *sox10*<sup>+</sup> and 0% sensory-related OLCs that were *mbpa*<sup>+</sup>, matching the *mbpa* expression in 5 dpf sensory-related OLCs (**Figure 6B**,  $n = 9$ , 15 dpf animals). We also quantified the marked *mbpa* expression in non-sensory-related OLCs (**Figure 6C**,  $n = 18$  animals total). We observed 25% of non-sensory-related OLCs were *mbpa*<sup>−</sup> while 75% of non-sensory-related OLCs were *mbpa*<sup>+</sup> at 5 dpf ( $n = 9$ , 5 dpf animals). Similarly at 15 dpf we observed 30% of non-sensory-related OLCs were *mbpa*<sup>−</sup> while 70% of non-sensory-related OLCs were *mbpa*<sup>+</sup> ( $n = 9$ , 15 dpf animals). To test that the lack of *mbpa* expression in sensory-related OLCs was not specific to the transgene, we also stained animals at 15 dpf with anti-MBPα (**Figure 6D**). At 15 dpf, there were an average of 0.0 ± 0 sensory-related OLCs expressing MBPα (per imaging window) compared to an average of 6.2 ± 1.2 non-sensory-related OLCs that were MBPα<sup>+</sup> (per imaging window) (**Figure 6E**,  $n = 4$  animals total,  $p = 0.0026$ ). These data are consistent with the possibility that sensory-related OLCs do not express myelin-associated factors at 5 dpf or 15 dpf, past the typical initiation period of ensheathment (Watkins et al., 2008; Czopka et al., 2013). It is important to note that although they do not express myelination components, it is unlikely that these cells



represent NG2 cells because of their expression of *nkx2.2*, which NG2 cells do not express (Hughes and Appel, 2016).

## Sensory-Related OLCs Display Distinct $\text{Ca}^{2+}$ Transients Than Non-sensory-related OLCs

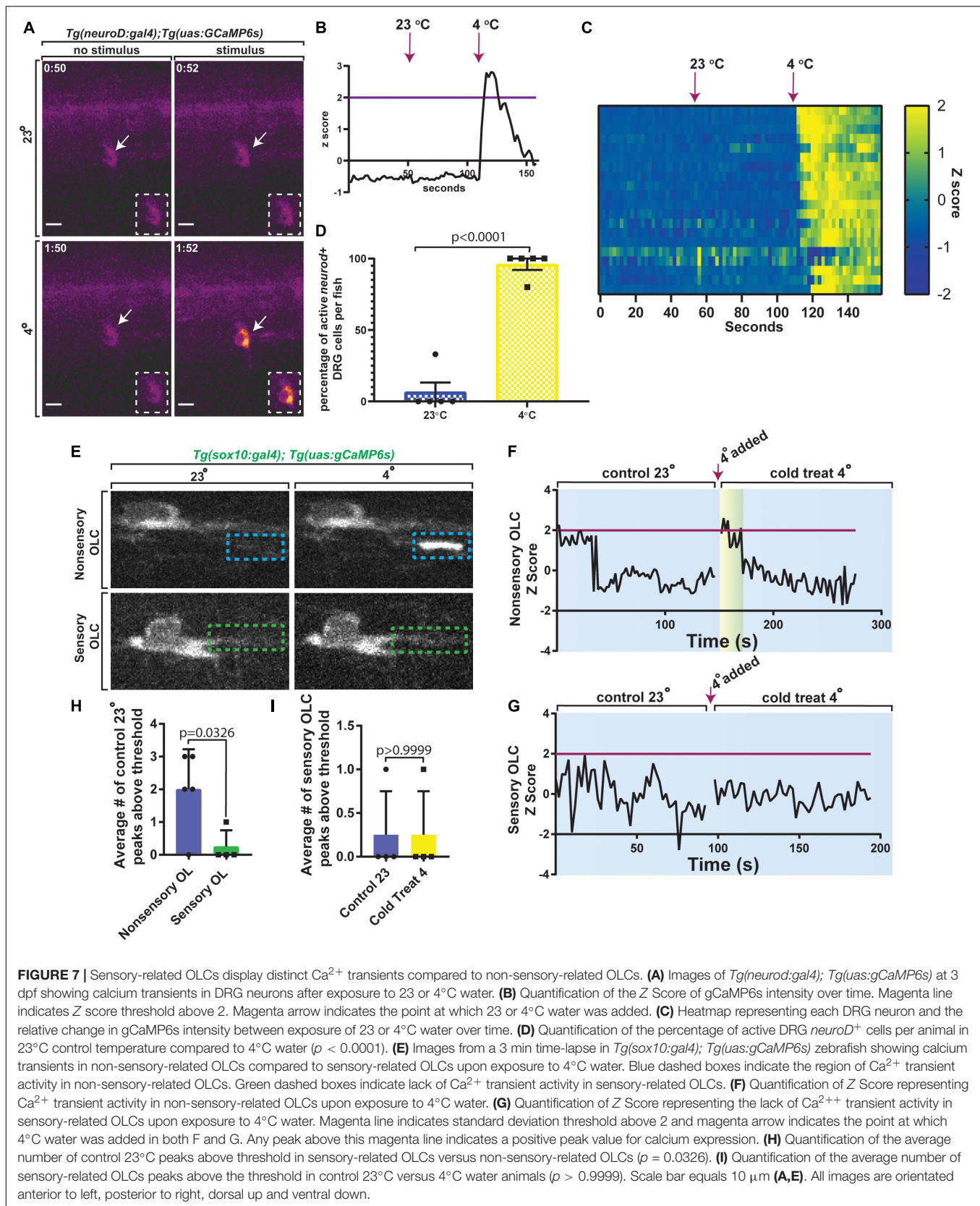
Oligodendrocytes have been shown to have both spontaneous and evoked  $\text{Ca}^{2+}$  transients. We next investigated such transients in sensory-related OLCs. DRG neurons can respond to a multitude of stimuli (Lumpkin and Caterina, 2007) and previous literature indicated DRG neurons could be active after exposure to 4°C (Fosque et al., 2015; Nichols and Smith, 2020). We first tested this by imaging *Tg(neurod:gal4)*; *Tg(uas:GCaMP6s)* and measured calcium transients in DRG neurons after exposure to 4 or 23°C water at 3 dpf ( $n = 21$  DRG cells). *Tg(neurod:gal4)*; *Tg(uas:GCaMP6s)* animals were anesthetized for mounting purposes then transferred back into 23°C water without anesthesia before the beginning of the assay ( $n = 5$  animals). Unanesthetized animals were imaged at 2 s intervals, imaged for 1 min, exposed to 23°C water, and then imaged for an additional 1 min, after which 4°C water was added followed by another 1 min of imaging (Figure 7A) ( $n = 21$  DRG cells). In this analysis, the Z score of DRG neuron integral densities were measured and used to assess significant changes in GCaMP6s intensity. If GCaMP6s integral density Z score was 2 or greater, this was marked as an active firing event (Figure 7B) ( $n = 5$  animals). To verify that this activation was consistent across multiple DRG, we created heat maps of each DRG neuron and their change in GCaMP6s intensity Z score at each timepoint (Figure 7C) ( $n = 5$  animals). Using a strict threshold to create a binary assessment of DRG activation, animals exposed to 4°C water resulted in a significant change in the percent of active DRG neurons at an average of 96% as compared to 6.6% activation in 23°C water (Figure 7D,  $p < 0.0001$ ,  $n = 5$  animals). These results are consistent with the hypothesis that zebrafish DRG neurons respond to 4°C.

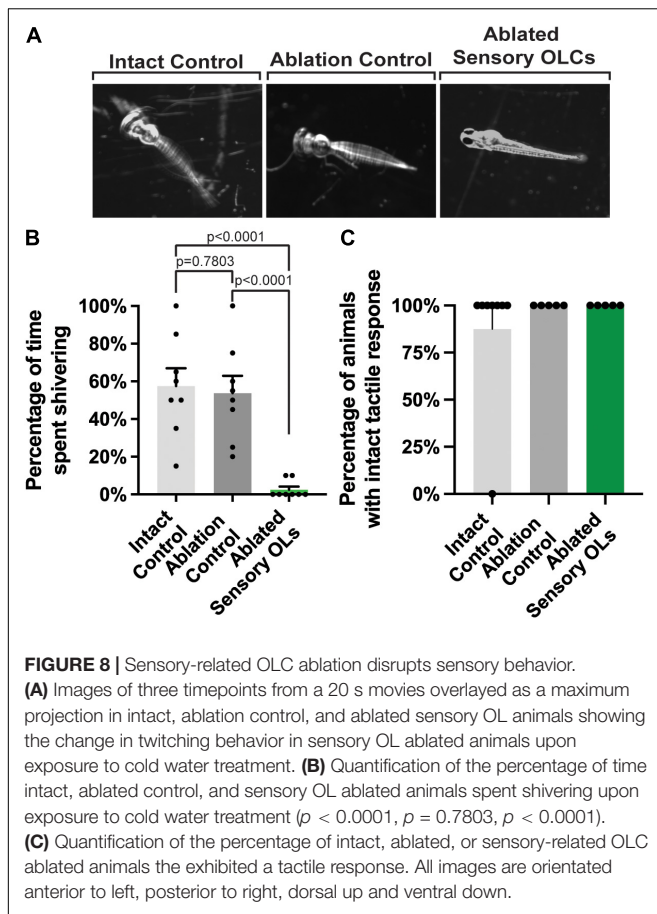
We therefore next tested if sensory-related OLCs display  $\text{Ca}^{2+}$  characteristics like non-sensory-related OLCs in both spontaneous and evoked scenarios (Krasnow et al., 2018; Marisca et al., 2020). We first asked if sensory-related OLCs display spontaneous activity like those described in previous reports (Hines et al., 2015; Mensch et al., 2015; Baraban et al., 2017; Krasnow et al., 2018; Marisca et al., 2020). To do this *Tg(sox10:gal4)*; *Tg(uas:GCaMP6s)* animals at 3 dpf were imaged. We first imaged baseline  $\text{Ca}^{2+}$  at 100 ms for 2 min in sensory-related OLCs at 23°C. These movies displayed full cell or sheath  $\text{Ca}^{2+}$  transients that could be detected in non-sensory OL but not sensory-related OLC (Figure 7E) ( $n = 9$  animals total). These data demonstrate that in homeostatic conditions, sensory-related OLC do not display spontaneous  $\text{Ca}^{2+}$  transients like non-sensory-related OLCs. We may, at the least, expect  $\text{Ca}^{2+}$  transients to be detectable upon evoking the sensory circuit. To test this we exposed animals to 4°C then measured GCaMP6s intensity in both sensory and non-sensory-related OLCs. Non-sensory-related OLCs displayed an immediate spike in  $\text{Ca}^{2+}$  transient activity upon exposure to 4°C (Figure 7F)

( $n = 5$  non-sensory-related OLCs). Alternatively, sensory-related OLCs did not display full cell/sheath  $\text{Ca}^{2+}$  transients after exposure to 4°C compared to 23°C (Figure 7G) ( $n = 4$  sensory-related OLCs). The average number of peaks with a Z score above 2 was significantly different from  $2.0 \pm 0.548$  in non-sensory-related OLCs compared to  $0.25 \pm 0.25$  in sensory-related OLCs (Figure 7H) ( $n = 9$  animals). We then compared the average number of peaks in sensory-related OLCs with a Z score above 2 in 23°C versus 4°C animals and there was no change and the Z scores remained at an average of  $0.25 \pm 0.25$  peaks above threshold, or a Z score below 2 (Figures 7G,I) ( $p > 0.9999$ ). These data demonstrate an additional distinct property of sensory-related OLCs from non-sensory-related OLCs.

## Sensory-Related OLCs Are Important for Somatosensory Responses

Our results indicate that sensory-related OLCs are located at specific locations in the spinal cord at 5–10 and 13–18 DRGs (Figure 1D). We, therefore, next considered the hypothesis that sensory-related OLCs may be required somehow in the sensory response. The DRG neurons fire upon immersion in 4°C, resulting in a hypothermic shivering behavior (Nichols and Smith, 2020; Kikel-Coury et al., 2021). To explore if sensory-related OLCs function in behavior, all detectable sensory-related OLCs on the right side of the animal were ablated at 3 dpf. Following ablation, animals were recovered for 24-h. All animals that were tested displayed an intact sensory axon. Animals with ablated sensory-related OLCs were compared to animals with no ablations. As an additional control that the ablation laser itself did not elicit a change in behavior, the exact laser parameters used to ablate sensory-related OLCs were exposed to a region 10  $\mu\text{m}$  from a sensory-related OLCs ( $n = 24$  animals total). These animals were then immersed in 4°C for 10 sec and the percent of time shivering was calculated. Intact animals displayed a stereotypical shivering for 57.5% of time (intact versus ablation control  $p = 0.7803$ ) ( $n = 8$  intact animals) (Figures 8A,B). A similar phenotype was observed with ablation controls displaying shivering for 53.75% of time (intact versus ablation control  $p = 0.7803$ ) ( $n = 8$  ablation control animals). This was in contrast to animals in which sensory-related OLCs were removed, which significantly reduced the shiver behavior to 2.5% of time spent shivering (intact versus ablated sensory  $p < 0.0001$ , ablation control versus ablation sensory  $p < 0.0001$ ) ( $n = 8$  ablated sensory-related OLC animals) (Figures 8A,B). To test if this eliminated other somatosensory responses, we performed an assay to determine an intact tactile response by touching the head of the animal with a pipette tip (Kikel-Coury et al., 2021; Figure 8C). Following this tactile assay, we could not detect differences in the percentage of intact, ablation control and sensory-related OLC ablated animals exhibiting a tactile response. 87.5% of intact control animals, 100% of ablation control animals, and 100% of ablated sensory-related OLC animals responded to the tactile assay (Figure 8C) ( $n = 24$  animals total). In zebrafish at 4 dpf, Rohon Beard and trigeminal neurons detect tactile responses while the DRG





do not (Ribera and Nuslein-Volhard, 1998). This indicates sensory-related OLCs could have a critical function in the DRG-specific behavioral circuit.

## DISCUSSION

Oligodendrocytes are essential for brain and spinal cord functionality (Nave and Werner, 2014; Allen and Lyons, 2018). In this study we demonstrate an OLC subpopulation that resides on the DRG axons in the spinal cord of zebrafish. These peripheral derived neurons provide a link between the CNS and PNS (Golding et al., 1997; Lumpkin and Caterina, 2007). Manipulations of DREZ genesis, where these DRG neurons cross from the periphery to the spinal cord, alters sensory-located OLCs. Artificial lesions that mimic a spinal cord axonal invasion supports the hypothesis that DREZ formation could be sufficient to impact these OLCs. Supporting a role of sensory-related OLCs in circuit function, ablation of sensory-related OLCs eliminates a DRG-specific somatosensory behavior (Nichols and Smith, 2020; Kikel-Coury et al., 2021). Together these data reveal a role for the DREZ in producing a unique OLCs population that functions in somatosensory neurons.

The traditional description of a mature oligodendrocyte is that it myelinates (Nave and Werner, 2014; Allen and Lyons, 2018). By the traditional definition, MBP-negative oligodendrocytes

are simply immature. For this reason, we conservatively refer to the cells we uncovered as sensory-related OLCs instead of mature OLs. Although this is one interpretation, another is that MBPa-negative oligodendrocytes are themselves mature oligodendrocytes with distinct functions. Pio del Rio Horteaga proposed such a possibility, describing cells associated with blood vessels and neuronal somata as non-myelinating oligodendrocytes (Rio-Hortega et al., 1921a; Sierra et al., 2016). Single-cell sequencing of oligodendrocyte cells also demonstrate subpopulations of cells that express myelin markers at undetectable levels (Marques et al., 2016). Schwann cells, which myelinate the PNS, also present in non-myelinating mature forms (Jessen and Mirsky, 1997, 2005). Nonetheless, non-myelinating oligodendrocytes remain poorly understood. Our data supports the possibility that *mbpa*-negative OLC could be present in the spinal cord of zebrafish, albeit in low abundance and at very specific locations. In zebrafish, studies have shown heterogeneity of *mbpa*-negative OLCs with one population representing a subgroup that has less complexity like we visualize (Marisca et al., 2020). The potential functional role of sensory-related OLCs in a DRG-specific circuit within that circuit underscores their importance, regardless if they are a mature oligodendrocyte or an immature, long-lived progenitor. It also remains a possibility that sensory-related OLCs do not express *mbpa* but do express *mbpb*, or other myelin proteins.

The results above demonstrate the DREZ is important to produce a subpopulation of OLCs in the zebrafish of the spinal cord. Although our data supports the model that sensory and non-sensory-related OLCs are derived from a similar population of precursors cells in the spinal cord, our experiments do not distinguish between the possibilities that sensory-related OLCs are generated from a progenitor population that is unspecified until the DREZ forms or if a population is pre-determined to arrive to the DREZ once it is formed. It is clear, however, that sensory-related OLCs are derived from the ventral spinal cord region, likely the pMN domain. In mice, the presence of oligodendrocytes that are labeled with traditional myelin markers inhibits synaptic presence in ectopically located somatosensory axons in Semaphorin 6D mutants, suggesting that oligodendrocytes can inhibit synapses and thereby could be hypothesized to be required for somatosensory behaviors (Leslie et al., 2011).

Although our study reveals an interesting interaction between the DREZ and OLCs, it opens a gap in what molecular components at the DREZ drive such events. Discovering such molecules will help to further delineate myelinating oligodendrocytes from those that do not express typical myelin markers. Given that breach alone was sufficient to induce such a sensory-related OLC state, it seems possible the molecules released after injury could be involved. We also identified that sensory-related OLCs contact the DREZ, indicating that both secreted and short-range cues could be involved in the development of sensory-related OLCs. Studies that outline oligodendrocyte responses to injury will also be important guides for such discovery of the DREZ cue.

Our results also indicate an interesting change in sensory-induced behavior when sensory-related OLCs are reduced. This

result was surprising given such a small number of ablated cells had such a profound impact on behavior. At the moment, our interpretation of that result is limited given the potential caveats of cell ablation in the intact spinal cord; although the control animals showed normal behavior. We also cannot explain why sensory-related OLCs appear at two areas of the spinal cord, especially given that spinal cord development should occur similarly on the anterior/posterior axis. However, the location of these cells in limited regions and the change in behavioral responses after their ablation could be linked. One possibility is that these cells function in synapse maturity of the sensory circuit and thus are located at regions where two neurons must be connected. It will be imperative to have a detailed and careful mapping of the sensory circuit in order to investigate such a possibility. Another possibility is that sensory-related OLCs tune the conduction velocity of DRG sensory neurons, akin to what is proposed in the auditory brainstem axons (Ford et al., 2015). However, we do not see changes in sheath length over 4 days. Regardless, it will be important in the future to further investigate the presumed impact on somatosensory driven behaviors. Our work demonstrates that sensory-related OLCs are MBPa<sup>-</sup> and have distinct Ca<sup>2+</sup> transients compared to non-sensory-related OLCs. Such data does not completely rule out the possibility that the sensory-related OLCs are in a different stage of differentiation compared to non-sensory-related OLCs. However, tracking sensory-related OLCs over a 4 day period did not show changes in sheathes, consistent to increased differentiation. We also did not see sensory-related OLCs express MBPa by 15 dpf. Investigation of the molecular determinants or markers of sensory-related OLCs will help to address the question of their differentiation state.

Our study establishes the role of PNS development in connectivity and function of the spinal cord, expanding the potential mechanisms that regulate OLC development. Collectively, the OLC heterogeneity in this study includes anatomical, structural, developmental and functional attributes.

## MATERIALS AND METHODS

### Ethics Statement

All animal studies were approved by the University of Notre Dame Institutional Animal Care and Use Committee.

### Contact for Reagent and Resource Sharing

Further information and requests for resources and reagents should be directed to the Lead Contact, CS. All of the data for this study is included in the figures.

### Experimental Model and Subject Details

All animal studies were approved by the University of Notre Dame IACUC as noted above. The following zebrafish strains were used in this study: AB, *Tg(sox10:mrfp)* (Kucenas et al., 2008), *Tg(sox10:megfp)* (Smith et al., 2014), *Tg(nkx2.2a:gfp)*

(Kirby et al., 2006), *Tg(sox10:eos)* (McGraw et al., 2012), *Tg(sox10:gal4;uas:lifeact-gfp)* (Helker et al., 2013; Hines et al., 2015), *Tg(gfap:nsfb-mcherry)* (Johnson et al., 2016; Smith et al., 2016), *Tg(olig2:dsred)* (Park et al., 2002), *Tg(dbx:gfp)* (Briona and Dorsky, 2014), *Tg(nbt:dsred)* (Peri and Nüsslein-Volhard, 2008), *Tg(ngn1:gfp)* (Prendergast et al., 2012), and *Tg(mbpa:gfp)* (Czopka et al., 2013). All germline transgenic lines used in this study were stable unless otherwise noted. Pairwise matings were used to produce embryos and raised at 28°C in egg water in constant darkness. Animals were staged by hours or days post fertilization (hpf and dpf) (Kimmel et al., 1995). Embryos of either sex were used for all experiments.

## Method Details

### In vivo Imaging

Animals were anesthetized using 3-aminobenzoic acid ester (Tricaine), covered in 0.8% low-melting point agarose. Animals were then mounted laterally on their right side in glass-bottomed 35 mm petri dishes (Nichols et al., 2018). Images were acquired on a spinning disk confocal microscope custom built by 3i technology (Denver, CO) that contains: Zeiss Axio Observer Z1 Advanced Mariana Microscope, X-cite 120LED White Light LED System, filter cubes for GFP and mRFP, a motorized X, Y stage, piezo Z stage, 20X Air (0.50 NA), 63X (1.15NA), 40X (1.1NA) objectives, CSU-W1 T2 Spinning Disk Confocal Head (50 μm) with 1X camera adapter, and an iXon3 1Kx1K EMCCD camera, dichroic mirrors for 446, 515, 561, 405, 488, 561,640 excitation, laser stack with 405 nm, 445 nm, 488 nm, 561 nm, and 637 nm with laser stack FiberSwitcher, photomanipulation from vector high speed point scanner ablations at diffraction limited capacity, Ablate Photoablation System (532 nm pulsed laser, pulse energy 60J @ 200 HZ). Images in time-lapse microscopy were collected every 5 min for 24 h or from 24 to 72 h depending on the experiment. Adobe Illustrator, ImageJ, and IMARIS were used to process images. Only brightness and contrast were adjusted and enhanced for images represented in this study. All fluorescence quantifications were normalized to the background value of each image.

### IMARIS Reconstructions

The surface renderings represented in this study were reconstructed using IMARIS version 9.6. We used the surfaces tool within IMARIS to generate surface renderings of raw volume confocal z-stack images (all 30 μm stacks for all reconstructed images). A smoothing detail of 0.200 μm within the surfaces feature was selected and kept consistent across all reconstructed images and no raw volume background values were adjusted when creating reconstructions. The threshold value for each experimental imaging group was selected to remove surface rendered background artifacts and include as much of the rendered OLCs as possible in the reconstructed image. Each threshold cutoff value was manually selected per experimental imaging group and kept consistent within each imaging group. These manual threshold values were set as 182.697 (Figure 2A), 298.637 (Figure 2D), 222.863 (Figure 2E), 376.059 (Figure 3E), and 358.236 (Figure 6A).

To create the cross sectional view represented in **Figure 2D**, we rotated the raw volume view of our image 90 degrees into the z-plane and set our slice position to visualize the right projection of a sensory related OLC. We then used the Ortho Slicer tool in the YZ plane with a slice step size of 1  $\mu\text{m}$  to obtain the slice view of that 1  $\mu\text{m}$  plane.

To create the surface rendering in **Figure 2D**, we created individual surfaces channels for the *Tg(ngn1:gfp)* and *Tg(sox10:mrfp)* channels. Following reconstruction, since the OLC and other *sox10* expression was labeled in the same channel, we grouped the reconstructed surface pixels that coincided with the raw volume view of the sensory related OLC and also grouped the reconstructed surface pixels that were not associated with the sensory related OLC. We then pseudo colored the two groups within the reconstructed *Tg(sox10:mrfp)* channel. Cyan represented the *sox10*<sup>+</sup> non-sensory related OLC and magenta represented the sensory related OLC. Similarly, we grouped the reconstructed surface pixels that coincided with the raw volume view of the sensory related OLC contacting the DREZ and grouped the pixels coinciding with the DRG in *Tg(sox10:gal4;uas:lifect-gfp)* represented in **Figure 3E**. Here we pseudo colored the DRG in gray and pseudo colored the sensory related OLC in green. The surface renderings represented in **Figures 2A,E, 6A** were also reconstructed using the surfaces tool in IMARIS following the noted smoothing details and thresholding values detailed above, however; no OLCs or structures were present within the same transgenic channel so no pixels were grouped or pseudo colored for these channels.

We did not perform any quantitative analysis using IMARIS software, instead we strictly used this software as a tool to allow for better visualization of small sensory related OLCs and their related structures. All quantifications were performed using ImageJ or Microsoft Excel described below in our quantitative analysis section.

### Single-Cell Ablations

*Tg(sox10:mrfp)*, and *Tg(sox10:megfp)* animals were anesthetized using 0.02% 3-aminobenzoic acid ester (Tricaine) in egg water. Fish were then mounted in 0.8% low-melting point agarose solution, arranged laterally on a 10 mm glass-coverslip bottom petri dish, and placed on the microscope anterior to posterior. Confocal z-stack images of sensory and non-sensory-related OLCs in individual transgenic animals at 72 hpf were taken pre-ablation. Confirmed sensory and non-sensory cells were brought into a focused ablation window. Upon focusing the confirmed cell, we double-clicked on the center of the cell body using a 4  $\mu\text{m}$  cursor tool to fire the laser (Nichols et al., 2018; Green et al., 2019). All laser parameters used are specific to our confocal microscope. Specific parameters include Laser Power (2), Raster Block Size (4), Double-Click Rectangle Size (8), and Double-Click Repetitions (4). 30  $\mu\text{m}$  z-stack images taken at a 1  $\mu\text{m}$  step size were then collected using time-lapse confocal microscopy every 5 min for 24 h or from 72 to 96 h.

### Single OL Imaging Over Multiple Days

Confocal z-stack images of *Tg(nkx2.2a:gfp);Tg(sox10:mrfp)* animals at 3 dpf were taken to locate and confirm the presence

of sensory-related OLCs. After locating a sensory-related OLC, we counted DRGs anteriorly from the DRG most adjacent to the sensory-related OLC. We also counted the somites of the animal anteriorly from the somite number most adjacent to the location of the sensory-related OLC. At 4 dpf, we used the DRG number and somite number to locate the same sensory-related OLC within the same animal. Upon locating the sensory-related OLC we took a confocal z-stack image. We repeated the location and imaging process at 5 dpf and 6 dpf. We quantified the length and width of sheaths of individual sensory-related OLCs over a 4-day period using ImageJ. We reconstructed these 30  $\mu\text{m}$  confocal z-stack images of sensory-related OLCs at each timepoint using the surfaces feature using IMARIS. We created individual surfaces channels for the green *Tg(nkx2.2a:gfp)* and pseudocolored cyan *Tg(sox10:mrfp)* channels. Following reconstruction we pseudocolored the sensory related OLC in magenta. All surfaces channels used a surface detail of 0.200  $\mu\text{m}$  and we did not adjust the background values within the surfaces feature.

### Chemical Treatments

The chemical treatments used for this study include SU6656 (Santa Cruz Biotechnology) and paclitaxel (Acros) (Nichols and Smith, 2019a). Stock solutions of both reagents were kept at 20°C. SU6656 was kept at a concentration of 375  $\mu\text{M}$ . Paclitaxel was kept at a concentration of 2.2 mM (Nichols and Smith, 2019a). All embryos were dechorionated at 36 hpf and incubated with 3  $\mu\text{M}$  (SU6656) and 22  $\mu\text{M}$  (paclitaxel) in egg water until imaging (Nichols and Smith, 2019a). All control animals were incubated with 1% DMSO in egg water.

### Dorsal Root Ganglia Ablations

*Tg(sox10:mrfp);Tg(ngn1:gfp)* 48 hpf animals were anesthetized using 0.02% 3-aminobenzoic acid ester (Tricaine) in egg water. Fish were then mounted in 0.8% low-melting point agarose solution, arranged laterally on a 10 mm glass-coverslip bottom petri dish, and placed on the microscope anterior to posterior. Following the formation of pioneer axons from the DRG, we selected an 8  $\mu\text{m}$  area between the DRG and the pioneer axon and double-clicked to fire the lesion laser (Nichols et al., 2018; Green et al., 2019). All laser parameters used are specific to our confocal microscope. Specific parameters include Laser Power (3), Raster Block Size (2), Double-Click Rectangle Size (8), and Double-Click Repetitions (4). Following DRG ablations, 30  $\mu\text{m}$  z-stack images taken at a 1  $\mu\text{m}$  step size were then collected using time-lapse confocal microscopy every 5 min for 24 h from 48 to 72 hpf.

### PA-Rac1

A *tol2-4xnr UAS-PA Rac1-mcherry* plasmid was diluted to 12 ng/ $\mu\text{l}$  in water along with 25 ng/ $\mu\text{l}$  of *transposase* mRNA. The injection solution was injected into *Tg(sox10:gal4);Tg(uas:lifect-GFP)* embryos. Embryos were screened for *mcherry* expression via confocal microscopy at 48 hpf. Mature PA-Rac1 photoactivates upon exposure to 445 nm light. We imaged *mcherry*<sup>+</sup> DRGs for 24 h with exposure to 445 nm light. As a control we imaged *mcherry*<sup>+</sup> DRGs for 24 h without exposure to 445 nm light. *tol2-4xnr UAS-PA Rac1-mcherry* was a gift from

Anna Huttenlocher (Addgene plasmid #41878) (Yoo et al., 2010). Light stimulation in non-paRac1 animals has no measurable impact (Yoo et al., 2010). Following PA-Rac1 treatment, 30  $\mu\text{m}$  z-stack images taken at a 1  $\mu\text{m}$  step size were then collected using time-lapse confocal microscopy every 5 min for 24 h from 48 to 72 hpf.

### Radial Glia Focal Lesion

Focal lesions of the radial glia membrane to mimic a DREZ injury were created using the Ablate!™ Photoablation System described above (Nichols and Smith, 2019a). Two laser induced lesions were created at 48 hpf. Each focal lesion ranged from 10 to 12  $\mu\text{m}$  in size and was created 10  $\mu\text{m}$  from the ventral radial glial membrane. This area best represented the location of the DREZ. Non-lesioned DREZ areas of adjacent nerves served as controls. Following laser induced focal lesioning, time-lapse images of the nerves were taken as described above for 24 h. Following radial glia focal lesion ablations, 30  $\mu\text{m}$  z-stack images taken at a 1  $\mu\text{m}$  step size were then collected using time-lapse confocal microscopy every 5 min for 24 h from 48 to 72 hpf.

### Immunohistochemistry

The primary antibody used to determine mature myelination was anti-*mbpa* (1:500, rabbit, Appel Lab) (Kucenas et al., 2009). The secondary antibody used was Alexa Fluor 647 goat anti-rabbit (1:600; Invitrogen). 15 dpf animals were fixed in 4% PFA in PBST (PBS, 0.1% Triton X-100) at 25°C for 3 h. Fixed animals were washed with PBST, DWT (dH<sub>2</sub>O, 0.1% Triton X-100), and acetone for 5 min each. Next, the animals were incubated in -30°C acetone for 10 min and then washed three times with PBST for 5 min each. Animals were then incubated with 5% goat serum in PBST for 1 h at 25°C, then the primary antibody solution was added for 1 h at 25°C. After 1 h, animals were transferred to 4°C overnight. Fixed animals were washed three times with PBST for 30 min each and once more for 1 h. Animals were then incubated with secondary antibody solution for 1 h at 25°C, then transferred to 4°C overnight. Fixed animals were washed three times with PBST for 1 h and immediately imaged. Animals were mounted, and confocal images were taken using the protocol above for *in vivo* imaging. 50  $\mu\text{m}$  still z-stack images taken at a 1  $\mu\text{m}$  step size were then collected using confocal microscopy.

### Calcium Imaging

*Tg(sox10:gal4);Tg(uas:gCaMP6s)* and *Tg(neurod:gal4);Tg(uas:gCaMP6s)* 3 dpf animals were mounted in 0.8% low-melting point agarose solution, arranged laterally on a 10 mm glass-coverslip bottom petri dish, and placed on the microscope anterior to posterior. Animals were not anesthetized. For neuronal imaging, spinal cord z-stacks were collected that spanned 10  $\mu\text{m}$  (1  $\mu\text{m}$  steps) and imaged for 3 min with 2 s intervals. For OLC imaging, confocal z-stack images of the spinal cord in individual transgenic animals at 3 dpf were taken to confirm the presence of sensory and non-sensory-related OLCs. Upon confirmation, sensory-related OLCs were imaged every 2 s for 2 min to capture Ca<sup>2+</sup> transients in room temperature (23 degree) egg water. After imaging baseline Ca<sup>2+</sup> activity, room temperature egg water was removed and 3 mL of 4 degree cold

egg water was added. Animals were then imaged immediately following the addition of 4 degree egg water and after refocusing. Non-sensory-related OLCs were also imaged every 2 s for 2 min as a control. The exposure was set to 100 ms.

### Animal Behavior After Sensory-Related OLC Ablations

*Tg(sox10:mrfp)* animals at 72 hpf were anesthetized using 0.02% 3-aminobenzoic acid ester (Tricaine) in egg water. Fish were then mounted in 0.8% low-melting point agarose solution, arranged laterally on a 10 mm glass-coverslip bottom petri dish, and placed on the microscope anterior to posterior. Confocal z-stack images of *Tg(sox10:mrfp)* animals at 72 hpf were taken to locate and confirm the presence of sensory-related OLCs. We ablated sensory-related OLCs using the Ablate!™ Photoablation Laser following the single-cell ablation methods described above. Following successful ablation, we unmounted individual animals from the agarose solution. We then placed individual animals into a small petri dish containing 4°C egg water and recorded their twitching response to cold water treatment for a 20 s period using an AxioZoom Observer microscope with ZenPro Image Acquisition software. As a control for the ablation, we ablated a small 4  $\mu\text{m}$  region above the sensory axon where a typical sensory OL would reside. As another control, we imaged a separate set of intact control animals that had unablated sensory-related OLCs. The ablated, ablated control, and intact control animals were each exposed to 4°C egg water and their twitching response to cold water treatment was recorded over a 20 s period using Zeiss ZenPro image acquisition software on a Zeiss Axio Observer microscope.

### Quantitative Analysis

#### Quantification and Statistical Analysis

To generate composite z-images for the cell, 3i Slidebook software (Denver, CO, United States) was used. Individual z-images were sequentially observed to confirm composite accuracy. All graphically presented data represent the mean of the analyzed data unless otherwise noted. Cell tracking was performed using the MTrackJ plugin for ImageJ<sup>1</sup>. GraphPad Prism software (San Diego, CA, United States) was used to determine statistical analysis. Full detail of the statistical values can be found in **Supplementary Table S1**.

#### Quantification of Direction Changes

To track the direction changes of OLCs, we imaged *Tg(sox10:mrfp)* and *Tg(sox10:gal4;uas:lifeact-gfp)* animals from 48 to 72 hpf. We then tracked single *sox10*<sup>+</sup> OLCs in each animal throughout the 24 time-lapse movie using the MTrackJ plugin of ImageJ. We quantified the total distance an individual OLC traveled as well as the amount of direction changes an individual OLC experienced throughout the 24-h imaging window.

#### Quantification of Migration

To track the individual paths of sensory and non-sensory-related OLCs, the MTrackJ plugin on ImageJ was used. The center of

<sup>1</sup><https://imagejscience.org/meijering/software/mtrackj/> (Bethesda, MD)

each cell body was traced over time, and quantitative data were collected by ImageJ. Resulting x and y coordinates of each cell were overlaid to create migration plots. All distance and time points were calculated by the MTrackJ software and further quantified using Microsoft Excel (Redmond, WA).

### K-Means Analysis

Oligodendrocyte lineage cells were clustered into three groups clustered based on their migration distance and number of direction changes from 48 to 72 hpf using *k*-means analysis in R. The *k* value was determined by the elbow method. Code is available in **Supplementary File 1**.

### Quantification of Sheath Length and Width

To determine the length and width of sensory and non-sensory OL sheaths, we used the freehand tracing tool in ImageJ. We traced the ensheathed area longitudinally and laterally and used the Analyze feature within ImageJ to obtain quantitative results.

### Quantification of Velocity

To obtain the velocity of an individual OLC traveling, we tracked individual paths of sensory and non-sensory-related OLCs throughout the timelapse imaging window using the MTrackJ plugin on ImageJ. We tracked the center of each cell body over time and used the quantitative distance and time collected by ImageJ to calculate velocity. We calculated the velocity using Microsoft Excel (Redmond, WA, United States).

### Quantification of OLC Projections

To determine the number of both sensory and non-sensory related OLC projections, we tracked individual OLCs throughout the 24-h timelapse imaging window from 48 to 72 hpf and counted the maximum number of extended projections each individual OLC created after migrating to the DREZ.

### Quantification of Calcium Imaging

We imaged *Tg(sox10:gal4);Tg(uas:gCaMP6s)* 3 dpf animals every 2 s for 2 min to visualize  $Ca^{2+}$  transient waves in sensory and non-sensory OLCs exposed to 4 and 23°C degree egg water. Later, we enlarged the movies to visualize one sensory or non-sensory-related OLC at a time. We used the line tool in ImageJ to trace individual projections of OLCs and then measured the integrated density along the projection using the integrated density tool within ImageJ. In order to assess changes in integrated density, we then used Microsoft Excel to calculate the *Z* score of the integrated density for each projection. Any *Z* score  $>$  or  $=$  2 were noted as positive for  $Ca^{2+}$  transient activity. Any *Z* score  $<$  2 were not recognized as positive for  $Ca^{2+}$  transient activity. We first tested this by imaging *Tg(neurod:gal4); Tg(uas:GCaMP6s)* and measured calcium transients in DRG neurons after exposure to 4 or 23°C water. We imaged *Tg(neurod:gal4); Tg(uas:gCaMP6s)* 3dpf animals every 2 s for 3 min to assess changes in gCaMP6s fluorescence of DRG neurons in response to 23 and 4°C egg water. Movies were analyzed in ImageJ by tracing individual DRG neuron somas and measuring integrated density for each timepoint. In this analysis, the *Z* score of DRG neuron integral densities were measured and used to assess changes in integral

density. If gCaMP6s integral density *Z* score was 2 or greater, this was marked as an active firing event.

### Quantification of Animal Behavior

We recorded the behavior of sensory ablated, ablation control, and intact animals for 20 s immediately following exposure to 4°C egg water. Any movies longer than 20 s were normalized to 20 s. We recorded the amount of time each animal spent shivering in cold water treatment. We divided the total time an animal spent shivering over the total time recorded. All calculations were performed using Microsoft Excel (Redmond, WA, United States).

## DATA AVAILABILITY STATEMENT

The original contributions presented in this study are included in the article/**Supplementary Material**, further inquiries can be directed to the corresponding author.

## ETHICS STATEMENT

The animal study was reviewed and approved by all animal studies were approved by the University of Notre Dame IACUC.

## AUTHOR CONTRIBUTIONS

LG, RG, JB, and EN conducted all experiments. LG, RG, JB, and CS analyzed all experiments. LG and CS wrote the manuscript with input from RG and JB. CS and LG conceived the project. All authors contributed to the article and approved the submitted version.

## FUNDING

This work was funded by the Alfred P. Sloan Foundation (CS) and the NIH (DP2NS117177). Further support was provided by the University of Notre Dame, the Elizabeth and Michael Gallagher Family, Garibaldi Family Endowment for Excellence in Adult Stem Cell Research, Center for Zebrafish Research at the University of Notre and Center of Stem Cells and Regenerative Medicine at the University of Notre Dame.

## ACKNOWLEDGMENTS

We thank David Lyons, Bruce Appel, and Ethan Scott for transgenic zebrafish lines, Bruce Appel, Jacob Hines, and members of the Smith and Wingert labs for their helpful comments. We also thank Sara Cole and the Notre Dame Imaging Core for their help using IMARIS software.

## SUPPLEMENTARY MATERIAL

The Supplementary Material for this article can be found online at: <https://www.frontiersin.org/articles/10.3389/fncel.2022.893629/full#supplementary-material>

## REFERENCES

- Allen, N. J., and Lyons, D. A. (2018). Glia as architects of central nervous system formation and function. *Science* 185, 181–185.
- Baraban, M., Koudelka, S., and Lyons, D. A. (2017). Ca<sup>2+</sup> activity signatures of myelin sheath formation and growth in vivo. *Nat. Neurosci.* 21, 19–23. doi: 10.1038/s41593-017-0040-x
- Briona, L. K., and Dorsky, R. I. (2014). Radial glial progenitors repair the zebrafish spinal cord following transection. *Exp. Neurol.* 256, 81–92. doi: 10.1016/j.expneurol.2014.03.017
- Cai, J., Qi, Y., Hu, X., Tan, M., Liu, Z., Zhang, J., et al. (2005). Generation of oligodendrocyte precursor cells from mouse dorsal spinal cord independent of Nkx6 regulation and Shh signaling. *Neuron* 45, 41–53.
- Crawford, A. H., Tripathi, R. B., Richardson, W. D., and Franklin, R. J. M. (2016). Developmental origin of oligodendrocyte lineage cells determines response to demyelination and susceptibility to age-associated functional decline. *Cell Rep.* 15, 761–773. doi: 10.1016/j.celrep.2016.03.069
- Czopka, T., Ffrench-Constant, C., and Lyons, D. A. (2013). Individual oligodendrocytes have only a few hours in which to generate new myelin sheaths in vivo. *Dev. Cell* 25, 599–609. doi: 10.1016/j.devcel.2013.05.013
- Emery, B. (2010). Regulation of oligodendrocyte differentiation. *Trends Neurosci.* 33, 359–362.
- Fogarty, M., Richardson, W., and Kessar, N. (2005). A subset of oligodendrocytes generated from radial glia in the dorsal spinal cord. *Development* 132, 1951–1959. doi: 10.1242/dev.01777
- Ford, M. C., Alexandrova, O., Cossell, L., Stange-Marten, A., Sinclair, J., Kopp-Scheinflug, C., et al. (2015). Tuning of Ranvier node and internode properties in myelinated axons to adjust action potential timing. *Nat. Commun.* 6:8073.
- Fosque, B. F., Sun, Y., Dana, H., Yang, C. T., Ohyama, T., Tadross, M. R., et al. (2015). Labeling of active neural circuits in vivo with designed calcium integrators. *Science* 347, 755–760. doi: 10.1126/science.1260922
- Golding, J., Shewan, D., and Cohen, J. (1997). Maturation of the mammalian dorsal root entry zone - from entry to no entry. *Trends Neurosci.* 20, 303–308. doi: 10.1016/S0166-2236(96)01044-1042
- Green, L. A., Nebiolo, J. C., and Smith, C. J. (2019). Microglia exit the CNS in spinal root avulsion. *PLoS Biol.* 17:e3000159. doi: 10.1371/journal.pbio.3000159
- Green, L., and Smith, C. J. (2018). Single-cell photoconversion in living intact zebrafish. *J. Vis. Exp.* e57024. doi: 10.3791/57024
- Green, L., and Smith, C. J. (2018). Single-cell photoconversion in living intact zebrafish. *J. Vis. Exp.* 57024. doi: 10.3791/57024
- Helker, C. S. M., Schuermann, A., Karpanen, T., Zeuschner, D., Belting, H.-G., Affolter, M., et al. (2013). The zebrafish common cardinal veins develop by a novel mechanism: lumen ensheathment. *Development* 140, 2776–2786. doi: 10.1242/dev.091876
- Hines, J. H., Ravanelli, A. M., Schwindt, R., Scott, E. K., and Appel, B. (2015). Neuronal activity biases axon selection for myelination in vivo. *Nat. Neurosci.* 18, 683–689. doi: 10.1038/nn.3992
- Hughes, E. G., and Appel, B. (2016). The cell biology of CNS myelination oligodendrocyte precursors and their distribution. *Curr. Opin. Neurobiol.* 39, 93–100. doi: 10.1016/j.conb.2016.04.013
- Hughes, E. G., Kang, S. H., Fukaya, M., and Bergles, D. E. (2013). Oligodendrocyte progenitors balance growth with self-repulsion to achieve homeostasis in the adult brain. *Nat. Neurosci.* 16, 668–676. doi: 10.1038/nn.3390
- Jessen, K. R., and Mirsky, R. (1997). Embryonic Schwann cell development: the biology of Schwann cell precursors and early Schwann cells. *J. Anat.* 191, 501–505. doi: 10.1017/S0021878297002434
- Jessen, K. R., and Mirsky, R. (2005). The origin and development of glial cells in peripheral nerves. *Nat. Rev. Neurosci.* 6, 671–682. doi: 10.1038/nrn1746
- Johnson, K., Barragan, J., Bashiruddin, S., Smith, C. J., Tyrrell, C., Parsons, M. J., et al. (2016). Gfap-positive radial glial cells are an essential progenitor population for later-born neurons and glia in the zebrafish spinal cord. *Glia* 64, 1170–1189. doi: 10.1002/glia.22990
- Kessar, N., Fogarty, M., Iannarelli, P., Grist, M., Wegner, M., and Richardson, W. D. (2006). Competing waves of oligodendrocytes in the forebrain and postnatal elimination of an embryonic lineage. *Nat. Neurosci.* 9, 173–179. doi: 10.1038/nn1620
- Kikel-Coury, N. L., Green, L. A., Nichols, E. L., Zellmer, A. M., Pai, S., Hedlund, S. A., et al. (2021). Pioneer axons utilize a Dcc signaling-mediated invasion brake to precisely complete their pathfinding odyssey. *J. Neurosci.* 41, 6617–6636. doi: 10.1523/JNEUROSCI.0212-21.2021
- Kimmel, C. B., Ballard, W. W., Kimmel, S. R., Ullmann, B., and Schilling, T. F. (1995). Stages of embryonic development of the zebrafish. *Dev. Dynam.* 203, 253–310. doi: 10.1002/aja.1002030302
- Kirby, B. B., Takada, N., Latimer, A. J., Shin, J., Carney, T. J., Kelsh, R. N., et al. (2006). In vivo time-lapse imaging shows dynamic oligodendrocyte progenitor behavior during zebrafish development. *Nat. Neurosci.* 9, 1506–1511. doi: 10.1038/nn1803
- Koudelka, S., Voas, M. G. G., Almeida, R. G. G., Baraban, M., Soetaert, J., Meyer, M. P. P., et al. (2016). Individual neuronal subtypes exhibit diversity in CNS myelination mediated by synaptic vesicle release. *Curr. Biol.* 26, 1447–1455. doi: 10.1016/j.cub.2016.03.070
- Krasnow, A. M., Ford, M. C., Valdivia, L. E., Wilson, S. W., and Attwell, D. (2018). Regulation of developing myelin sheath elongation by oligodendrocyte calcium transients in vivo. *Nat. Neurosci.* 21, 24–30. doi: 10.1038/s41593-017-0031-y
- Kucenas, S., Takada, N., Park, H. C., Woodruff, E., Broadie, K., and Appel, B. (2008). CNS-derived glia ensheath peripheral nerves and mediate motor root development. *Nat. Neurosci.* 11, 143–151. doi: 10.1038/nn2025
- Kucenas, S., Wang, W.-D., Knapik, E. W., and Appel, B. (2009). A selective glial barrier at motor axon exit points prevents oligodendrocyte migration from the spinal cord. *J. Neurosci.* 29, 15187–15194.
- Leslie, J. R., Imai, F., Fukuhara, K., Takegahara, N., Rizvi, T. A., Friedel, R. H., et al. (2011). Ectopic myelinating oligodendrocytes in the dorsal spinal cord as a consequence of altered semaphorin 6D signaling inhibit synapse formation. *Development* 138, 4085–4095. doi: 10.1242/dev.066076
- Lumpkin, E. A., and Caterina, M. J. (2007). Mechanisms of sensory transduction in the skin. *Nature* 445, 858–865. doi: 10.1038/nature05662
- Marisca, R., Hoche, T., Agirre, E., Hoodless, L. J., Barkey, W., Auer, F., et al. (2020). Functionally distinct subgroups of oligodendrocyte precursor cells integrate neural activity and execute myelin formation. *Nat. Neurosci.* 23, 363–374. doi: 10.1038/s41593-019-0581-582
- Marques, S., Zeisel, A., Codeluppi, S., Bruggen, D., Van, Falcão, A. M., et al. (2016). Oligodendrocyte heterogeneity in the mouse juvenile and adult central nervous system. *Science* 352, 1326–1329. doi: 10.1126/science.aaf6463
- McGraw, H. F., Snelson, C. D., Prendergast, A., Suli, A., and Raible, D. W. (2012). Postembryonic neuronal addition in Zebrafish dorsal root ganglia is regulated by Notch signaling. *Neural Dev.* 7:23. doi: 10.1186/1749-8104-7-23
- Mensch, S., Baraban, M., Almeida, R., Czopka, T., Ausborn, J., El Manira, A., et al. (2015). Synaptic vesicle release regulates myelin sheath number of individual oligodendrocytes in vivo. *Nat. Neurosci.* 18, 628–630. doi: 10.1038/nn.3991
- Naruse, M., Ishino, Y., Kumar, A., Ono, K., Takebayashi, H., Yamaguchi, M., et al. (2016). The dorsoventral boundary of the germinal zone is a specialized niche for the generation of cortical oligodendrocytes during a restricted temporal window. *Cereb. Cortex* 26, 2800–2810.
- Nave, K. A., and Werner, H. B. (2014). Myelination of the nervous system: mechanisms and functions. *Annu. Rev. Cell Dev. Biol.* 30, 503–533.
- Nichols, E. L., and Smith, C. J. (2019a). Pioneer axons employ Cajal's battering ram to enter the spinal cord. *Nat. Commun.* 10:562. doi: 10.1038/s41467-019-08421-8429
- Nichols, E. L., and Smith, C. J. (2019b). Synaptic-like vesicles facilitate pioneer axon invasion. *Curr. Biol.* 29, 2652–2664.e4.
- Nichols, E. L., and Smith, C. J. (2020). Functional regeneration of the sensory root via axonal invasion. *Cell Rep.* 30, 9–17.e3. doi: 10.1016/j.celrep.2019.12.008
- Nichols, E. L., Green, L. A., and Smith, C. J. (2018). Ensheathing cells utilize dynamic tiling of neuronal somas in development and injury as early as neuronal differentiation. *Neural Dev.* 13:19. doi: 10.1186/s13064-018-0115-118
- Park, H., Mehta, A., Richardson, J. S., and Appel, B. (2002). olig2 is required for zebrafish prim ary motor neuron and oligodendrocyte development. *Dev. Biol.* 368, 356–368.
- Peri, F., and Nüsslein-Volhard, C. (2008). Live imaging of neuronal degradation by microglia reveals a role for v0-ATPase a1 in phagosomal fusion in vivo. *Cell* 133, 916–927. doi: 10.1016/j.cell.2008.04.037
- Prendergast, A., Linbo, T. H., Swarts, T., Ungos, J. M., McGraw, H. F., Krispin, S., et al. (2012). The metalloproteinase inhibitor Reck is essential for zebrafish DRG development. *Development* 139, 1141–1152. doi: 10.1242/dev.072439

- Ravanelli, A. M., and Appel, B. (2015). Motor neurons and oligodendrocytes arise from distinct cell lineages by progenitor recruitment. *Genes Dev.* 29, 2504–2515. doi: 10.1101/gad.271312.115
- Ribera, A. B., and Nuslein-Volhard, C. (1998). Zebrafish touch-insensitive mutants reveal an essential role for the developmental regulation of sodium current. *J. Neurosci.* 18, 9181–9191.
- Richardson, W. D., Kessaris, N., and Pringle, N. (2006). Oligodendrocyte wars. *Nat. Rev. Neurosci.* 7, 11–18. doi: 10.1038/nrn1826
- Río-Hortega, P. (1921a). Estudios sobre la neuroglía. La glía de escasas radiaciones (oligodendroglí). *Bol. Soc. Esp. Hist. Nat.* 21, 63–92.
- Sierra, A., de Castro, F., del Río-Hortega, J., Rafael Iglesias-Rozas, J., Garrosa, M., and Kettenmann, H. (2016). The “Big-Bang” for modern glial biology: translation and comments on Pío del Río-Hortega 1919 series of papers on microglia. *Glia* 64, 1801–1840. doi: 10.1002/glia.23046
- Smith, C. J., Johnson, K., Welsh, T. G., Barresi, M. J. F., and Kucenas, S. (2016). Radial glia inhibit peripheral glial infiltration into the spinal cord at motor exit point transition zones. *Glia* 64, 1138–1153. doi: 10.1002/glia.22987
- Smith, C. J., Morris, A. D., Welsh, T. G., and Kucenas, S. (2014). Contact-Mediated inhibition between oligodendrocyte progenitor cells and motor exit point glia establishes the spinal cord transition zone. *PLoS Biol.* 12:e1001961. doi: 10.1371/journal.pbio.1001961
- Smith, C. J., Wheeler, M. A., Marjoram, L., Bagnat, M., Deppmann, C. D., and Kucenas, S. (2017). TNF $\alpha$ /TNFR2 signaling is required for glial ensheathment at the dorsal root entry zone. *PLoS Genet.* 13:e1006712. doi: 10.1371/journal.pgen.1006712
- Spassky, N., Goujet-Zalc, C., Parmantier, E., Olivier, C., Martinez, S., Ivanova, A., et al. (1998). Multiple restricted origin of oligodendrocytes. *J. Neurosci.* 18, 8331–8343. doi: 10.1523/jneurosci.18-20-08331.1998
- Spitzer, S. O., Sitnikov, S., Kamen, Y., Faria, O., De, Agathou, S., et al. (2019). Oligodendrocyte progenitor cells become regionally diverse and heterogeneous with age article oligodendrocyte progenitor cells become regionally diverse and heterogeneous with age. *Neuron* 101, 459–471.e5. doi: 10.1016/j.neuron.2018.12.020.
- Tripathi, R. B., Clarke, L. E., Burzomato, V., Kessaris, N., Anderson, P. N., Attwell, D., et al. (2011). Dorsally and ventrally derived oligodendrocytes have similar electrical properties but myelinate preferred tracts. *J. Neurosci.* 31, 6809–6819. doi: 10.1523/JNEUROSCI.6474-10.2011
- Vallstedt, A., Klos, J. M., and Ericson, J. (2005). Multiple dorsoventral origins of oligodendrocyte generation in the spinal cord and hindbrain. *Neuron* 45, 55–67.
- Watkins, T. A., Emery, B., Mulinyawe, S., and Barres, B. A. (2008). Distinct stages of myelination regulated by  $\gamma$ -Secretase and astrocytes in a rapidly myelinating CNS coculture system. *Neuron* 60, 555–569. doi: 10.1016/j.neuron.2008.09.011
- Yoo, S. K., Deng, Q., Cavnar, P. J., Wu, Y. I., Hahn, K. M., and Huttenlocher, A. (2010). Differential regulation of protrusion and polarity by PI(3)K during neutrophil motility in live zebrafish. *Dev. Cell* 18, 226–236. doi: 10.1016/j.devcel.2009.11.015
- Zhang, Y., Nichols, E. L., Zellmer, A. M., Guldner, I. H., Kankel, C., Zhang, S., et al. (2019). Generating intravital super-resolution movies with conventional microscopy reveals actin dynamics that construct pioneer axons. *Development* 146:dev171512. doi: 10.1242/DEV.171512

**Conflict of Interest:** The authors declare that the research was conducted in the absence of any commercial or financial relationships that could be construed as a potential conflict of interest.

**Publisher’s Note:** All claims expressed in this article are solely those of the authors and do not necessarily represent those of their affiliated organizations, or those of the publisher, the editors and the reviewers. Any product that may be evaluated in this article, or claim that may be made by its manufacturer, is not guaranteed or endorsed by the publisher.

Copyright © 2022 Green, Gallant, Brandt, Nichols and Smith. This is an open-access article distributed under the terms of the Creative Commons Attribution License (CC BY). The use, distribution or reproduction in other forums is permitted, provided the original author(s) and the copyright owner(s) are credited and that the original publication in this journal is cited, in accordance with accepted academic practice. No use, distribution or reproduction is permitted which does not comply with these terms.